

Department of Materials Imperial College London

MEng Thesis Polytypism in halide perovskite solar cells

Caroline Boule

Supervisor: Prof. Aron Walsh
Group advisors: Mr. Jacob Wilson and Dr. Samantha Hood
External collaborator: Prof. Jisang Park (Kyungpook National University)
Assessors: Prof. David Dye and Dr. Johannes Lischner

Date of submission: 1st of June 2020

Abstract

Important challenges for halide perovskites consist of the stabilisation of their photoactive black phase at room temperature, and accordingly, the impediment of the transformation to the yellow phase occurring at lower temperatures. This transformation is particularly problematic when solar cells are scaled up; an important efficiency drop is observed. Polytypism represents one of the reasons for this efficiency drop, thus understanding how it influences the phase stability of halide perovskites is of paramount importance for fabrication of efficient, reproducible and scalable halide perovskite solar cells. In this project, a perovskite polytype builder was created using the Atomic Simulation Environment package. 2H, 3C, 4H, 6H and 12H polytypes were generated for the CsPbI₃ halide perovskite, the Cs₂Pb₂I₆ double perovskite, and for the three oxide perovskites, namely SrTiO₃, LaCoO₃, and KTaO₃. Electrostatic calculations were conducted on the structures using the Ewald method, to study the phase stability of the materials. It was found that the most stable polytype was the cubic 3C followed by the 12H, 6H, 4H and finally 2H, contradicting experimental observations. It has been concluded that a model considering electrostatics solely is too simplistic for the study of stability in halide perovskites; future models would be expected to be tuned with the inclusion of vibrational and configurational entropy.

Contents

1	Aims and Context	4
2	Literature Review	5
2.1	Motivation	5
2.2	Fundamentals of solar cells	5
2.3	Notable achievements to date	9
2.4	Halide perovskite solar cells	12
2.5	Halide perovskite phase stability and scaling challenges	15
2.6	Polytypism in halide perovskites	18
2.7	Summary	20
3	Methods	21
3.1	Creation of the perovskite polytype builder	21
3.2	Electrostatic energy calculations	21
3.3	Equilibrium distribution	23
4	Results and Discussion	23
4.1	Structure models and ranking for CsPbI ₃	23
4.2	Comparison to oxide perovskites	24
4.3	Application to double perovskites	25
4.4	Discussion of the model limitations	25
5	Conclusions (and suggestions for further work)	28
6	Appendix	34
6.1	Annotated polytype building code	34
6.2	Ewald summation method used to calculate electrostatic energy.	34
6.3	Boltzmann Population Distribution Calculations.	34

Collaboration and supervision

This is a new project, thus most results and methods presented in this report are new to this project. However, Prof Jisang Parks, a former postdoc of the group provided a code for generating the polytype structure.

Acknowledgements

I would like to express my gratitude towards Prof. Aron Walsh for his supervision and advice throughout the project and its write-up. I would also like to thank Dr. Samantha Hood for her valuable coding advice, and Mr. Jacob Wilson for helping me with the interpretation of my results. Thank you to Prof. Jisang Park from the Kyungpook National University for sharing his polytype builder with me which enabled me to run further calculations.

Finally, I would like to thank all the Materials Design group members for making me feel welcome and giving me an insight into their research which has allowed me to develop a love for photovoltaics.

1 Aims and Context

5 Metal halide perovskites are the breakthrough solar energy materials of the 21st century due to their efficient conversion of sunlight to electricity, and low cost deposition using scalable processes. However, the non-uniformity of the materials result in a rapid decline of the device efficiency when scaled up to larger areas. This project addressed one of the main obstacles: polytypism.

10 In tetrahedral semiconductors such as Si, GaN and ZnS, there is a well known competition between FCC (ABCABC) and HCP (ABAB) stacking sequences. Some materials favour zincblende (ABCABC), others favour wurtzite (ABAB), while often stacking faults form irregular repeating patterns (e.g. ABCABABC). A similar competition in stacking sequences has recently been found in halide perovskites, notably for formamidinium lead iodide which has close competition between a PV active black (ABCABC) and yellow (ABAB) phase that does not exhibit PV properties.

15 The aim of this project was to develop a python perovskite polytype builder, which can generate arbitrary stacking sequences of the perovskite structure. Electrostatic calculations were then to be applied to a selection of polytypes to compare their phase stability. The main assumption was that the phase stability of halide perovskites is governed by electrostatics. Experimentally, it has been observed that the 2H polytype, representing the yellow phase, dominates at room temperature and that the photoactive black phase could be achieved by heating. The purpose was to build a model which would give similar results to those observed
20 experimentally for the synthesized polytypes, and to expand the calculations to generated polytypes that have not been observed experimentally yet.

2 Literature Review

2.1 Motivation

A large part of the energy produced nowadays comes from the burning of fossil fuels. These produce greenhouse gases responsible for one of the main challenges the world is facing today: climate change [1]. Emissions from fossil fuel combustion and industrial processes contributed about 78% of the total greenhouse gas emissions increase from 1970 to 2011 with a total CO₂ emission increase of about 90% [2]. To tackle the problem, scientists are working towards a transition to renewable energy sources of which solar power generation has shown significant promise, partially due to the abundance of sunlight. The estimated world energy consumption in 2004 was 15TW, while 100% of the sun's incident energy was 174PW [3]. Therefore, all our consumption could potentially be supplied by solar energy. This clean source of energy is spreading rapidly, mainly due to the decreasing prices of its materials, and increasing availability.

2.2 Fundamentals of solar cells

2.2.1 Solar cell geometry and working principles

A solar cell (SC) is a solid-state electrical device that uses the photovoltaic (PV) effect to convert light energy into electrical energy [4]. The PV effect is a physical and chemical phenomenon that generates voltage and electric current in a material upon exposure to light. It is present in some semiconducting materials which have a conductivity between that of conductors and insulators, due to the size of their bandgap, smaller than that of conductors but larger than in insulators. Electrons can be thermally excited from the valence band to the conduction band, therefore resistivity drops with increasing temperature. The semiconductor conducting properties can be altered by doping it with positive or negative ions. When a doped semiconducting material contains high concentration of holes it is known as "p-type", and when it contains mostly free electrons it is called "n-type". Many p- and n-type regions can be present in a single semiconductor crystal. The junction between a p- and an n-type material is called a p-n junction and is responsible for the useful electronic behavior.

The photo-generated current is created when an incident photon is absorbed, generating an electron-hole pair which can be separated and collected by a p-n junction to prevent the carrier recombination that would lead to a loss of the electron-hole pair and no current generation. Electron-hole pairs are generated in solar cells if the incident photon has an energy greater than that of the band gap. However, electrons in the p-type material and holes in the n-type material only exist, before recombination, for a length of time on average equal to the minority carrier lifetime. The carriers are separated by an electric field existing at the p-n junction. The electrons in excess in the n-type material try to diffuse towards the p-type material while the excess holes in the p-type material try to diffuse towards the electrons in the n-type material. An electric field and a depletion region are formed at the junction due to the movement of electrons towards the p-type side exposing positive ion cores in the n-type side and the movement of holes to the n-type side that exposes negative ion cores in the p-type side. If the light-generated minority carrier reaches the p-n junction, the electric field sweeps it across the junction where it becomes a majority carrier. If the solar cell is short-circuited by the emitter and base connected together, then the light-generated carriers flow through the external circuit.

A simple solar cell is therefore composed of a p-type and an n-type material forming a p-n junction and covered with an anti-reflection coating to prevent the reflection of sunlight which would result in a loss of energy. Electrical contacts are used to connect a solar cell to the receiver of the produced current or to other solar cells [5]. PV systems used to power devices or heat water are composed of a number of solar panels, each combining solar modules which in turn consist of many solar cells, for which the composition is visible on Figure 1a.

2.2.2 Important solar cell properties

When comparing solar cell performance and photon-to-current conversion efficiency (PCE), several parameters listed below are important.

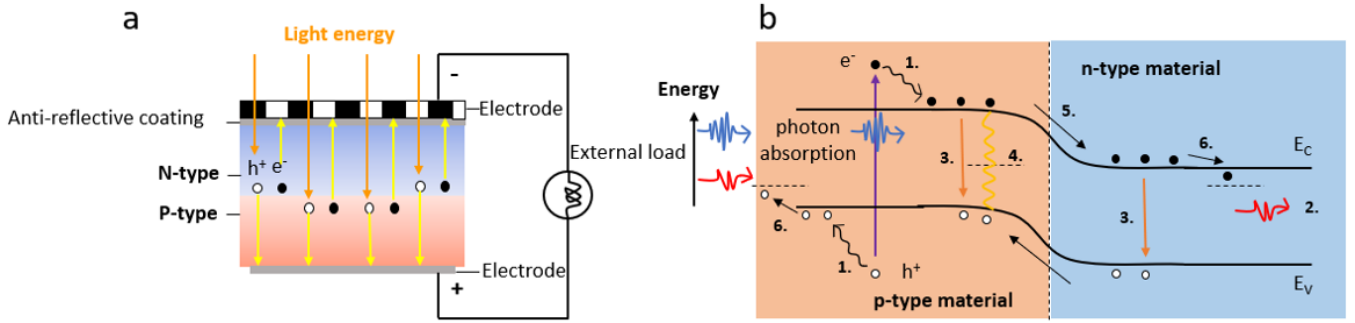


Figure 1: a) Sketch of the cross-section of a solar cell under operation [7] b) Model of a p-n junction solar cell showing the main mechanisms upon absorption of photons: (1) above band-gap/thermalisation, (2) below band-gap/transmission, (3) radiative recombination, (4) non-radiative recombination, (5) diffusion across the junction, (6) voltage drop at the contacts. (Adapted from [8]).

Band gap (E_g)

The photon energy is directly proportional to the photon's electromagnetic frequency as described by the Planck-Einstein relation (Eq. 2).

$$E = hf \quad (1)$$

Where h is the Planck constant and f the electromagnetic frequency. As $f = c/\lambda$, it can be simplified to:

$$E = \frac{hc}{\lambda} \quad (2)$$

Where c is the speed of light and λ is the wavelength. The photon energy is therefore inversely proportional to the photon's wavelength.

The entire spectrum of sunlight covers a range from approximately 0.5eV to 2.9eV. Photons with energy smaller than the semiconductor's E_g are not absorbed and pass through the cell. Thus, to absorb as much of the solar spectrum as possible, and therefore maximise the photocurrent produced by the device, a material with small E_g is required. However, this is counterbalanced by the desire to also have a large built-in voltage, which requires a larger E_g . The energy of photons above the bandgap is re-emitted as heat or light and materials with larger E_g lose less energy by thermal dissipation of excess photon energy. Ultimately, those two processes need to be balanced to optimise the solar cell efficiency, with an E_g usually between 1.0 and 1.7eV [5, 6].

Short-circuit current density (J_{SC})

The short-circuit current (I_{SC}) is the maximum current from a solar cell and occurs when the voltage across the device is zero (i.e., when the solar cell is short-circuited) as illustrated in Figure 2.

To remove the dependence of the solar cell area, it is more common to use the short-circuit current density (J_{SC}) in mA/cm². J_{SC} is due to the generation and collection of light generated carriers (holes and electrons) in a process described in 2.2.1. For an ideal solar cell, J_{SC} should be equal to the light-generated current density, which is the generation rate, multiplied by the probability of collection.

The factors that will impact J_{SC} are the number of photons (i.e., the power of the incident light source), the spectrum of the incident light (for most solar cell measurements, the spectrum is standardised to the AM 1.5 spectrum), the optical properties (absorption and reflection) of the solar cell, and the collection probability of the solar cell which in turn depends on the surface passivation, the minority carrier lifetime

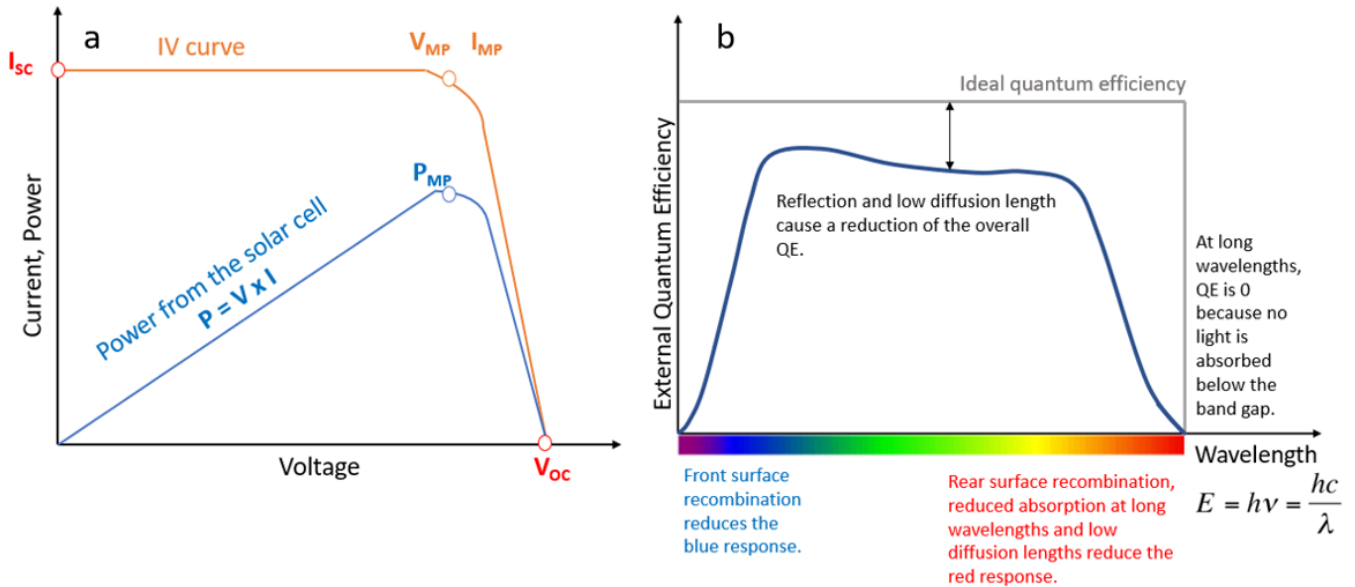


Figure 2: a) Solar cell current voltage (IV) curve with visible I_{SC} and V_{OC} . For maximum power output, the solar cell needs to operate at the maximum power point, PMP. b) Quantum efficiency of a silicon solar cell. It is usually not measured much below 350nm because the power from the AM 1.5 contained in such short wavelengths is low. (Adapted from [5]).

105 and the optical properties of the active layer.

To compare J_{SC} in solar cells of the same material type, the most important material parameters are the diffusion length and surface passivation. In a cell with perfectly uniform generation and passivated surface, the equation for J_{SC} can be approximated by:

$$J_{SC} = qG(L_n + L_p) \quad (3)$$

110

Where G is the generation rate, and L_n and L_p are the electron and hole diffusion lengths, respectively[5].

Open circuit voltage (V_{OC})

115 The open-circuit voltage (V_{OC}) is the maximum voltage available from a solar cell and occurs at zero current (see Figure 2a). It corresponds to the amount of forward bias in the solar cell due to the bias of the solar cell junction under the light-generated current. It indicates the amount of recombination occurring in the device. In most semiconductors, the maximum V_{OC} corresponds to the band gap. A lower V_{OC} indicates the presence of recombination. V_{OC} is derived from the splitting of the quasi-energy levels of
120 electrons in the conduction band and holes in the valence band. These quasi-energy levels are mathematical tools to describe the density of states which describes the charge carrier density when the charge carrier state is displaced from equilibrium. A larger splitting corresponds to a larger (V_{OC})

It can be calculated using the following equation [5]:

$$V_{OC} = \frac{nkT}{q} \ln\left(\frac{I_L}{I_0} + 1\right) \quad (4)$$

125

Where k is the Boltzmann constant, T represents the temperature, I_L and I_0 are respectively the light generated and dark saturation currents, and n is the ideality or efficiency factor.

Quantum efficiency (QE)

130

The quantum efficiency of a solar cell describes the ratio of the number carriers collected by the solar cell to the number of photons of a given energy incident on the solar cell. It can be given as a function of energy

or wavelength. The QE for photons with energy below E_g is zero, and it is equal to unity if all photons of a certain wavelength are absorbed and the minority carriers collected. In an ideal case, the QE as a function of the wavelength would give a square shaped curve visible on Figure 2b representing 100% absorption of photons with wavelengths ($E = hf$) above its band gap. However, in real materials the efficiency is reduced due to recombination effects.

Two types of QE can be measured:

- **Internal QE:** efficiency with which photons that are not reflected or transmitted out of the cell can generate collectable carriers.
- **External QE:** includes the effect of optical losses such as transmission and reflection[5].

Fill factor (FF)

The fill factor (FF) is a parameter which determines the maximum power from a solar cell. It is defined as the ratio of the maximum power from the solar cell to the product of V_{OC} and I_{SC} , the short-circuit current. Graphically on the IV curve, the FF measures the squareness of the solar cell and is the area of the largest rectangle. The FF value in devices is decreased by series and shunt resistance [5].

These parameters are directly or indirectly related to the solar cell efficiency, n , defined by:

$$n = \frac{V_{OC}I_{SC}FF}{P_{in}} \quad (5)$$

where P_{in} is the incident power.

2.2.3 Solar cell limits

Shockley - Queisser limit

Shockley–Queisser limit also known as the detailed balance limit [9], and first calculated by William Shockley and Hans Queisser in 1961, represents the maximum theoretical efficiency as a function of E_g of a solar cell made from a single p-n junction solar cell illuminated by a black body with a surface temperature of 6000K [9]. It is calculated from the amount of electrical energy extracted per incident photon. The maximum efficiency of a single-junction solar cell as calculated by the Shockley-Queisser model, is a function of bandgap energy. Recent calculations have placed the maximum solar conversion efficiency at around 33.7% with a bandgap of 1.4eV using an AM 1.5 solar spectrum which is the air mass coefficient chosen for standardised measurements of solar cells [10].

There are three primary considerations taken into account in the calculations of the Shockley-Queisser limit: (i) blackbody radiation, (ii) recombination, (iii) spectrum losses.

- **Blackbody radiation** Energy in the form of electromagnetic radiation is emitted by all objects with a temperature above absolute zero (0K). A blackbody is a theoretical body model which absorbs all radiation falling on it, without any reflection or transmission. Thus it is a perfect absorber and emitter over all wavelengths. The spectral distribution of the thermal energy radiated by a blackbody, which is the pattern of intensity of the radiation over a range of wavelengths or frequencies, only depends on temperature. At room temperature, the blackbody radiation from the solar cell cannot be captured by the cell and represents about 7% of the available incoming energy. As the energy lost in a cell is generally turned into heat, any inefficiency in the cell will increase the cell temperature when it is placed in sunlight. The blackbody radiation increases with the temperature of the cells until equilibrium is reached. Normally, this equilibrium is reached at temperatures as high as 360K, thus cells usually operate at lower efficiencies than their room temperature rating.
- **Recombination** Recombination processes such as those visible on Figure 1b, place an upper limit on the rate of electron-hole production which limits V_{OC} . For example, in silicon, recombination reduces the theoretical performance under normal operating conditions by another 10% over and above the thermal losses.

- **Spectrum losses** These limit J_{SC} as there are fewer photons above the bandgap at higher bandgaps. About 19% of solar radiation of the $1,000\text{W}/\text{m}^2$ in AM 1.5 has less than 1.1eV of energy and will not produce power in a silicon cell. This accounts for about 33% of the incident sunlight thus there is a theoretical conversion efficiency of about 4% from spectrum losses alone, ignoring all other factors.

185 Optical losses

The electrons and holes generated when incident photons pass through a semi-transparent charge transport material and arrive at the active layer of a solar cell can either diffuse towards the anode (electrons) or cathode (holes), or undergo some form of radiative or non-radiative recombination.

190

Radiative recombination occurs when electrons, which have been promoted to the conduction band and are in an excited, metastable state, return to the valence band to reduce their energy, and recombine with previously generated holes, leading to the emission of a photon.

195

Non-radiative losses take place when a photon with an energy below E_g is absorbed. As it cannot generate an electron-hole pair heat will be produced. Similarly, the absorption of a photon above E_g contributes to heat generation by converting the excess energy into kinetic energy of the carrier combination and as the carrier velocity decays to the drift velocity, there is phonon interaction. When an electron and a hole produce a photon equal to E_g during their recombination, it will contribute to losses in the cell unless it is reabsorbed. Inhomogeneities in the lattice such as defects and stacking faults may also contribute to non-radiative recombination mechanisms by creating energy levels in the band gap in which charge carriers will recombine.

200

Cost limitations

205

The first solar cells created required the use of ultra pure silicon, and the cost of materials and processing of the wafers was very large. This prevented the use of such solar cells as popular alternatives to fossil-fuel-based energy sources such as thermal power generation. However, the cost of PV has dropped by 74% since 2010 with a present cost below 0.05 USD per kWh of electric power. This can be compared with the fossil fuel-fired electricity cost range, which in 2017 was estimated to range from a low of 0.05 USD per kilowatt-hour (kWh) to a high 0.17 USD/kWh, depending on the fuel and country. Renewables and amongst them PV, are predicted to become globally more cost efficient than fossil fuels in the next few years [11].

210

215

A lot of research has therefore been conducted to search for cost-effective alternatives, leading to cheaper third-generation photovoltaics, including organic solar cells and dye-sensitized solar cells (DSSCs) [12]. A recent forecast predicted that PV will contribute nearly a third of new electricity generation capacity worldwide between now and 2030. This could be achieved by the development of more efficient and cost-effective solar cells, and by substantial reductions in the manufacturing costs of mainstream silicon solar cell technology [13].

220

However, materials costs are not the only ones and to reduce the overall cost of PV energy other costs need to be considered. These include logistics, operation and maintenance, lifespan, site preparation, working capital, grid connection, auxiliary equipment etc. [14]

225

2.3 Notable achievements to date

2.3.1 First generation solar cells

The first generation of solar cells, made from silicon are the oldest and commercially dominant PV technology. They are produced on wafers and can be monocrystalline or polycrystalline [15, 16]. Silicon solar cells cover 80% of the world installed capacity today. For more than 30 years, this technology has dominated the industry, with improvements through reduced cell thickness, especially during the silicon supply crisis in 2006-2008, and increased cell size. Although the basic cell structure remained unchanged over three decades, other improvements resulted in improving the cell efficiency from 11% to nearly 20% by 2018.

230

235 These improvements included an increased number of busbars, the switch to silicon nitride antireflection coatings and most substantially, from progressive incremental improvements to screen-printing pastes [17].

240 However, silicon technologies encountered a lot of issues related to wafer-Si solar cells the main ones being high production cost due to wafer cost, complicated manufacturing processes, and high thermal budget (1100°C) for an extended period of time (60min) [18]. Reflection, absorption and recombinational losses were also problems. Efficiency issues in multi-crystalline and amorphous silicon based cells were also present due to their disordered nature [19]. Moreover, ultra-high-purity silicon, obtained by crystallization of melted Si in a furnace at more than 1400°C, is required. The resulting high cost of materials and processing of the wafers, has prevented the popularisation of such solar cells as alternatives to fossil-fuel-based energy sources [12]. Varying the kind of material was one of the research solutions that scientists considered, leading to the birth of the second generation solar cells.

2.3.2 Second generation solar cells

250 The next generation of solar cells are thin film solar cells, made from semiconductor materials only a few micrometers thick. The main types of cells in this category are amorphous silicon, cadmium telluride/cadmium sulfide (CdTe/CdS) and copper indium gallium selenide (CIGS). Second generation materials have been developed to address production costs and energy requirements of first generation cells. Production costs are dominated by constituent material requirements. As manufacturing techniques evolve, some alternative techniques such as vapour deposition, electroplating, and use of Ultrasonic Nozzles have become advantageous due to the significant reduction of temperature that they offer during processing [20]. These thin films can also be grown on flexible substrates and thin film solar cells can be grown on large areas [15, 16, 21].

255 These technologies hold a promise of higher conversion efficiencies and offer significantly cheaper production costs and less material used, however their commercialisation has been proven difficult [20], partially due to the scarcity and toxicity of some of the materials used. CdTe module disposal is an issue since these modules cause pollution during decommissioning due to the toxicity of Cadmium. The main issue with CIGS solar cells is the price of indium [18].

2.3.3 Third generation solar cells

260 A lot of research has therefore been devoted to finding cheaper, high performance alternatives, leading to the third generation PV. New generation PV materials include nanotubes, polymers, organic dyes, conductive plastics, silicon wires, and solar inks using conventional printing press technologies. These technologies are promising but not commercially proven yet, the most developed 3rd generation solar cell being the dye sensitized solar cells (DSSC) also called Grätzel cells. They are based on dye molecules between electrodes. Electron hole pairs appear in those dye molecules and are transported through TiO₂ nanoparticles. They can have different colours and their cost is very low, but so is their efficiency. A large amount of solar radiation is concentrated onto a small region in concentrated cells, another promising technology in which the amount of semiconducting material is reduced, significantly reducing material costs [15, 16, 21].

275 In 2005-2006, while DSSC was being further developed, the use of an organic-inorganic lead halide perovskite as an absorber to replace the organic dye, was explored. That material opened a whole new research field, to exploit its semiconducting properties [12]. With a remarkable increase in conversion efficiency from about 3% in 2006 to over 24% in 2019, perovskite solar cells (PSCs) are the most promising 3rd generation technology.

2.3.4 The development of perovskites

280 Perovskites derive their name from the mineral structure of calcium titanium oxide (CaTiO₃), discovered by German mineralogist Gustav Rose in the year 1839, and which structure was characterised by a Russian mineralogist called Lev A. Perovski [22]. In 1893, Wells et al. performed a comprehensive study on the synthesis of lead halide compounds from solutions including lead halide and caesium, CsPbX₃ (X = Cl, Br, I), ammonium (NH₄), or rubidium, RbPbX₃ [23]. In 1957, C.K. Møller found that CsPbCl₃ and CsPbBr₃ have a tetragonally distorted perovskite structure which undergoes a transition to a pure cubic phase at

Major activities

2005	Prof Tsutomu Miyasaka, Dr Kojima and Dr Teshima begin the journey with perovskite photovoltaics
April 2009	First report on perovskite solar cell (3.8% efficiency), Miyasaka et al.
Nov 2012	Reports from H.Snaith and N.G. Park (above 10% efficiency)
2013-2015	<ul style="list-style-type: none"> Materials selection and process development for high efficiency Developing methods for high quality perovskite film formation Addressing issues of hysteresis, interfacial engineering
2016-2017	<ul style="list-style-type: none"> Compositional engineering of perovskite Improvement in both efficiency and stability Enhanced structural stability Increased effort in Pb-free perovskites
2018-now	<ul style="list-style-type: none"> Long term stability as major concern Addressing issues of moisture, thermal and photo instability Attempts being made to scale up Increased interests in inorganic halide perovskites

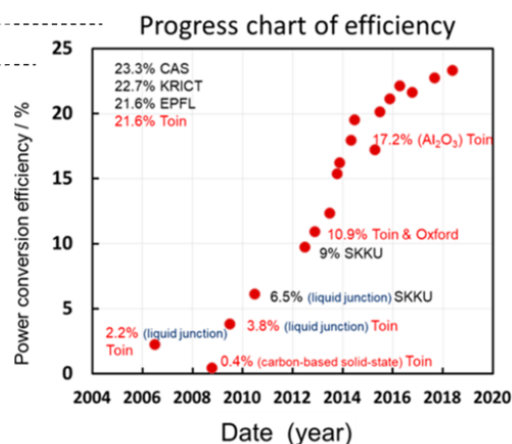


Figure 3: Milestones of progress in perovskite solar cells. (Adapted from [12]).

high temperatures [12, 24, 25]. The simple solution to synthesise these caesium lead halide ionic crystals might have inspired researchers such as Weber to use other cations instead of Cs and towards the end of the 20th century, a large variety of halide perovskites were synthesized by David Mitzi using small and large organic cations [26–28].

In 2009, Kojima et al replaced dyes in DSSCs by organic-inorganic halide perovskites, and fuelled an activity surge in the field of lead halide perovskites as photon harvesting materials when they achieved an efficiency of 3.8% [29]. A quantum-dot-sensitized solar cell with an efficiency of 6.5% was produced by Park et al by modulating the electrolyte synthesis route and the deposition of MAPbI₃ quantum dots onto a nanocrystalline TiO₂ layer, proving that perovskites could be serious competitors as potential light harvesters in solar cell applications. A significant progression in PSC was replacing the liquid electrolyte by a solid-state hole transmission material (HTM) using MAPbI₃ nanoparticles acting as the sensitizer to produce holes and electrons, and deposited onto a submicron-thick mesoscopic TiO₂ film with pores infiltrated with a hole-conductor spiro-MeOTAD forming a superstructured scaffold with a new PCE record of 9.7% [30, 31]. The following research conducted led to the creation, by Heo et al., of a 3-D composite TiO₂/MAPbI₃ device changing the polymer-based HTM's to achieve a 12% PCE with PTAA, resulting in a higher V_{OC} and FF than that of the previously used spiro-OMeTAD. In this device, the perovskite infiltrates the mesoporous TiO₂ structure layered on a compact TiO₂ sheet. The TiO₂ acts as an electron transmission material (ETM), and a HTM is used on top of the perovskite to complete the n-i-p junction. These structures continued to be developed, producing devices with efficiencies exceeding 20% [32].

Significant progress was made with the discovery of the perovskite's ambipolar nature to diffuse electrons and holes over distances exceeding 1 μ m, implying that a single planar perovskite layer is possible [33]. A new field of research was born aiming to create planar heterojunction hybrid inorganic/organic perovskite solar cells with low recombination probability and a high charge mobility in the perovskite leading to a high diffusion distance and carrier lifetime. Current records for planar perovskite devices are around 21%, but the stability of these devices is controversial [34]. To deliver more power, another absorber material can be combined in the perovskite solar cell, forming a high-performance tandem device. Perovskite solar cells are very efficient in converting visible and ultraviolet light into electricity making them excellent tandem partners with materials that convert low-energy light such as crystalline silicon. Tandem cells with silicon have demonstrated an efficiency of 28% [17]. Perovskite materials also have tunable bandgaps, which could lead to even higher-efficiency and more cost-effective tandem applications by custom-designing to complement the absorption of the partner material.

The milestones of progress of PSCs, reproduced from A. K. Jena et al. is visible on Figure 3. However, a number of challenges remain before they can become a competitive commercial technology as both their internal and external stabilities are limited. The potential environmental impacts of the lead-based

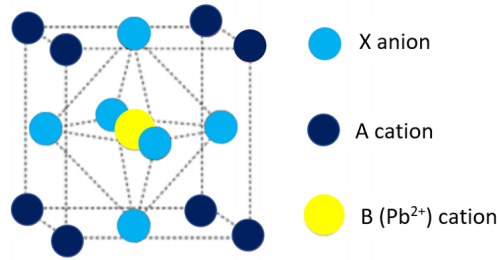


Figure 4: Crystallographic structure of a lead halide perovskite. (Adapted from [12]).

perovskite absorber represent additional barriers to commercialization. Studies are being conducted to reduce or eliminate the potential toxicity and environmental concerns. A final and important challenge faced by perovskite solar cells lies in the scale-up, reproducibility and optimization of the fabrication processes [35].

325

2.4 Halide perovskite solar cells

Metal halide perovskites are the breakthrough solar energy materials of the 21st century, efficiently converting sunlight to electricity, and with the possibility to be deposited at low cost using scalable processing. Halide perovskites of different structures exist, and have different associated properties.

2.4.1 Halide perovskite structure

A perovskite has a crystal structure of the form ABX_3 , in which A and B are cations and X is an anion typically oxygen, halogens, or alkali metals. In an ideal cubic structure, the B cation is surrounded by an octahedron of anions and has a 6-fold coordination; whereas the A cation has a 12-fold cuboctahedral coordination. In a cubic unit cell, A cations sit at cube corners, B at the body-centered position, and the X anion occupies the face-centered positions [12]. Due to their versatility, perovskites can form multidimensional structures using various combinations of different components [22].

335

Oxide perovskite were first discovered and mainly studied for their superior ferroelectric, magnetic, and superconductive properties [22]. They are used in various ferroelectric, piezoelectric, dielectric and pyroelectric applications. However, in most cases, they do not exhibit suitable semiconducting properties for PV applications. Nevertheless, when the oxide anions are replaced by halide anions, a class of halide perovskite is formed, which presents desired semiconducting properties for PV applications. The structure formed can be observed on Figure 4. Varying halide components to achieve different spectral responses can tune the photoconductive properties.

345

2.4.2 Different types of halide perovskite solar cells

Despite the existence of different types of perovskites and different cell architectures, their general working principle (see Figure 5a-c) stays the same. Electrons and holes are generated after the perovskite absorbs light and are selectively collected by the n-type and p-type transport material layers for electrons and holes respectively. Electrons then flow through the external circuit to combine with the holes in the p-layer. Carriers in perovskites demonstrate an unusual behavior as proven by the lack of a clear trend and the dispersion of V_{OC} dependences on different selective contacts. In general, organic-inorganic hybrid perovskites demonstrate numerous unusual photophysical characteristics, which result in excellent PV properties in the device [12].

355

All-inorganic halide perovskites

Organic-inorganic hybrid perovskites such as $MAPbI_3$ and $FAPbI_3$, and mixed-cation-based perovskites are leading in terms of efficiency. However, their long-term stability remains an issue as the organic cation (MA or FA) is responsible for poor thermal and environmental stability of these materials [36]. Therefore, replacement of the organic cation with an inorganic cation such as caesium (Cs^+) has been considered as

360

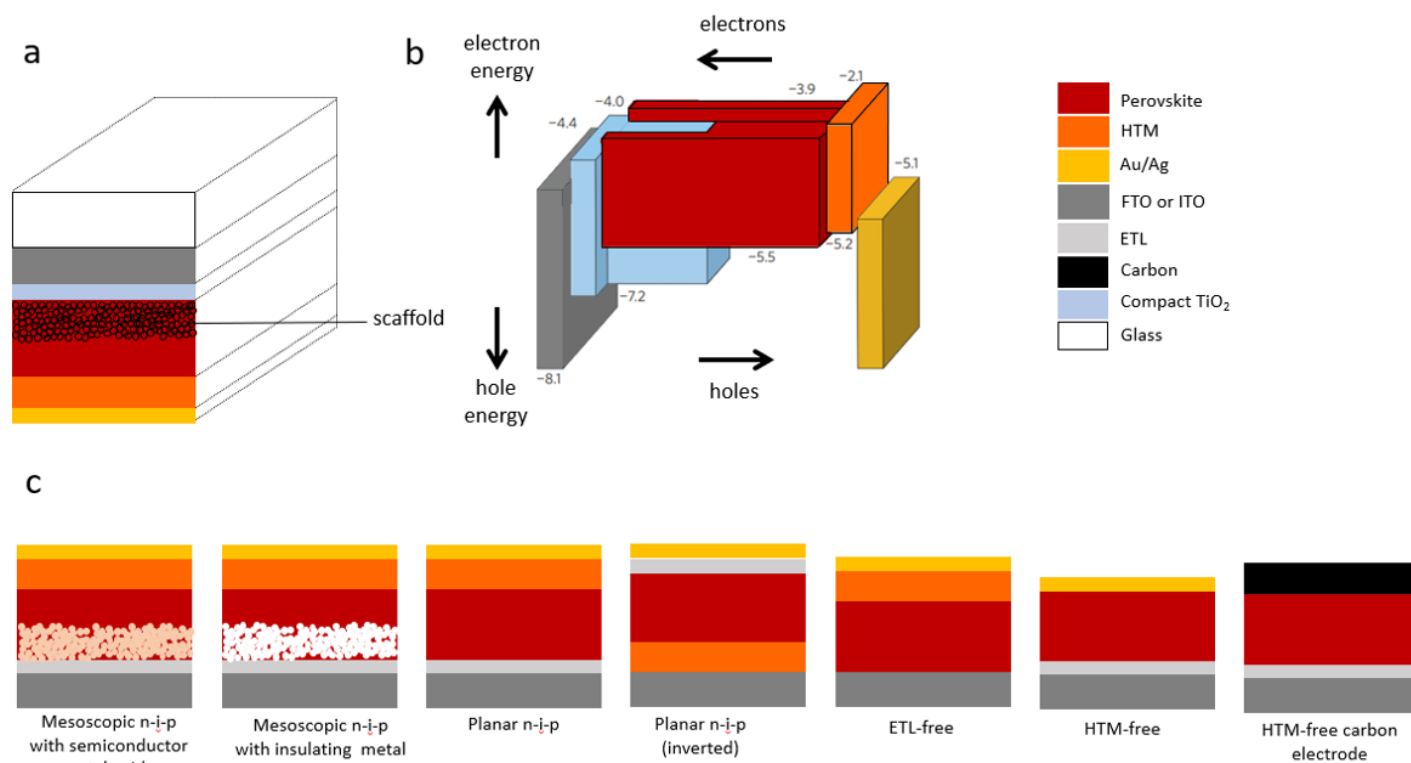


Figure 5: PSC structures with associated vacuum energy levels (Adapted from [12, 13]). a) General organic-inorganic halide solar cell including two optional layers not essential for high performance but with an energy of over 15% was reported for devices containing both optional layers with only the scaffold layer infiltrated by the perovskite (and then by the HTM) and without scaffolding, the structure then corresponds to a simple planar thin film cell. b) Vacuum energy levels (in eV) corresponding to $\text{CH}_3\text{NH}_3\text{PbI}_3$ perovskite and conducting TiO_2 . c) Different types of perovskite solar cell architectures. Here FTO is a Fluorine-doped Tin Oxide, ITO is the Indium tin oxide, and ETL means electron-transport layer.

a good solution to improve the perovskite's stability. First halide perovskite structures studied by Wells et al. in 1983, these caesium-based perovskite structures like CsPbX_3 and CsSnX_3 ($X = \text{Cl}, \text{Br}, \text{I}$) have been considered as model compounds among all-inorganic perovskites with their bandgap controlled by the halide ions. Despite its superior heat stability, CsPbI_3 has its own challenges, such as degrading into non-perovskite structures, which resulted in a slow progress of its PCE from 2.9% achieved by Snaith et al. [37] to reach 15.7% recently in a work undertaken by Pengyang et al. [38].

Hybrid organic-inorganic halide perovskites

Hybrid organic-inorganic perovskites are composed of an organic compound on the A-site instead of a single cation, a divalent B site cation and monovalent X-site halide anion. Compounds which adopt this structure are considered as very promising and include methylammonium lead iodide $\text{CH}_3\text{NH}_3\text{PbI}_3$ (MAPbI₃), methylammonium lead bromide ($\text{CH}_3\text{NH}_3\text{PbBr}_3$ (MAPbBr₃)), formamidinium lead iodide ($\text{HC}(\text{NH}_2)_2\text{PbI}_3$, (FAPbI₃)), and chloride-doped MAPbI₃ ($\text{CH}_3\text{NH}_3\text{PbI}_{3-x}\text{Cl}_x$). This family has an excellent combination of properties necessary for a remarkable absorber with an appropriate bandgap (1.4 - 1.5 eV), a high coefficient of absorption near ($10^4 - 10^5 \text{cm}^{-1}$), exceptional carrier transport, low exciton binding energy ($< 50 \text{meV}$), easily modulated properties through simple compositional modifications and compatibility with low-cost, large-area deposition techniques [39].

Mixed perovskites are now being investigated, in order to improve the properties of more familiar perovskites. Lead-free and low lead perovskites are also being studied because of that material's toxicity, which causes moral and environmental issues. Other interesting perovskite solar cells include the 1D and 2D technologies.

385 2.4.3 Halide perovskite enabling attributes

The solid-state physics of halide perovskites have only been investigated in details recently, despite its early discovery and the extensive work on the synthesis of lead halide perovskites. Theoretical and experimental intensive investigations carried out in recent years on semiconducting properties and carrier transport mechanism of these materials, pointed out the excellent PV application of 3D perovskite materials. They show exceptionally high power conversion efficiency and V_{OC} due to the material's remarkably superior properties. These include a high absorption coefficient ($\alpha > 105\text{cm}^{-1}$), a very long carrier diffusion length [13, 33, 40], a long carrier lifetime [41], a moderate carrier mobility [42–44], an unusually high suppressed recombination (defect tolerance), a slow carrier recombination [44], and a well-balanced charge transfer. Density functional theory (DFT) and first-principle theory-based calculations have been applied to support and explain the superior photophysical properties revealed by optoelectronic measurements [33, 42].

Despite being ionic crystals, halide perovskites exhibit semiconducting properties just like conventional semiconductors, which are usually covalent compounds (Si, CdTe, GaAs, etc.). Their optical absorption wavelength varies largely depending on the kind and the molar ratio of halides (I, Br, Cl) present in the structure. Therefore, the double ionic and semiconducting nature of perovskites allow the band gap and optical absorption to be easily tuned by varying the halide ions. Mixed-halide solids can be formed for that purpose by mixing I and Br or Cl and Br. It was observed for example that the absorption edge wavelength corresponding to the band gap energy of the mixed-halide material changed proportionally to the content of bromide and that when iodine was added to the perovskite structure, $\text{HC}(\text{NH}_2)_2\text{PbBr}_{1-y}\text{I}_y$, both the absorption and the emission exhibited a constant red peak shift [12, 45, 46].

Many halide perovskites, such as Methylammonium (MA) lead iodide ($\text{CH}_3\text{NH}_3\text{PbI}_3$, abbreviated as MAPbI_3), a standard perovskite absorber in PV cells, are intrinsic semiconductors exhibiting excellent mobility of photogenerated electrons and holes [47]. The high symmetry, direct band gap and p–p electronic transitions from valence band (VB) to conduction band (CB), enabled by the Pb s orbital lone pair, contribute to exceptionally high optical absorption coefficients of this material (105cm^{-1}) [13].

As an intrinsic semiconductor, MAPbI_3 has ambipolar carrier mobility and exhibits similar effective mass values for both electrons and holes [48], a rare property attributed to this ionic crystal. Photogenerated carriers behave as free carriers similarly to the ones in inorganic PV semiconductors, and can migrate in the perovskite absorber layer without recombination for a long time with PL measurements showing carrier lifetime of several hundreds of nanoseconds [33, 49, 50]. High ionic density in halide perovskites is also considered to help suppressing recombination between electrons and holes by a charge-screening effect against Coulombic interaction.

Defects act as recombination sites. However, halide perovskites are defect-tolerant due to strong Pb s–I p antibonding coupling, weak Pb p–I p coupling, and its ionic characteristics [51]. The lower valence band maximum (VMB) close to the I p orbital is lowered by the strong Pb s–I p antibonding coupling, while the weak antibonding coupling between Pb p and I p orbitals fixes the conduction band minimum (CBM) close to the Pb p orbital. Thus for vacancies formed by removal of I^- , the defect state lies between the Pb p atomic orbital level and the CBM, while the defect state for the Pb^{2+} vacancy is formed between the I p and VBM levels. Therefore, ion vacancies in perovskites generate trap states that reside within the VB or CB, or exist as shallow traps near the bands instead of forming traps deep within the band gap as it is the case for other ionic semiconductors where localized nonbonding orbitals surround the ion vacancies. When trapped in shallow defects, carriers can be detrapped easily and contribute to current generation. This results in a defect-tolerant nature of perovskites, which properties are not affected much by defect formation. It is reflected by the large carrier diffusion lengths, measured over the PL lifetime in the range 1–100 μm depending on the polycrystallinity [33, 52].

Despite the defect-tolerance of halide perovskite crystals, their defect (trap) density which is estimated to be from 10^{10}cm^{-3} in single crystals [52, 53] to 10^{16}cm^{-3} for polycrystals [49, 54] does to an extent limit the V_{OC} and efficiency. Therefore, to further improve efficiency, defects and traps should be reduced with pure solution-processed polycrystalline films. Losses caused by interfacial recombination are equally important and depend on the properties of other layers in the device. Therefore it is important for further improvements to understand the standard architecture and how to optimise electron and hole transport [12].

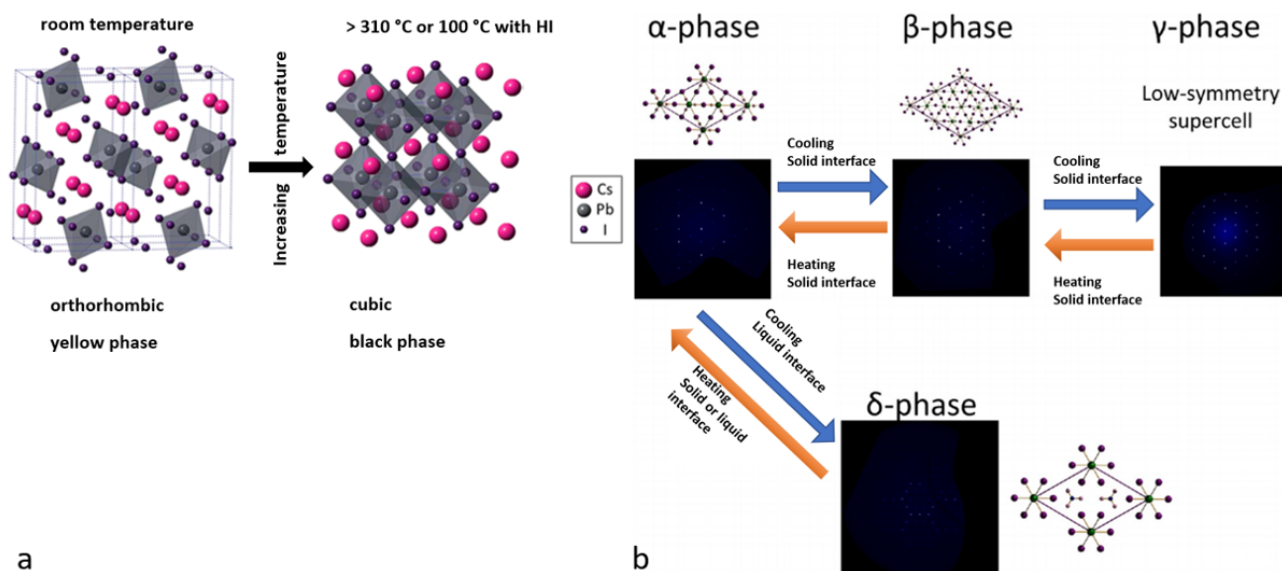


Figure 6: a) Crystal structures of both yellow and black phases of CsPbI₃. Adapted from [37]. b) Phase transitions observed in Pb and Sn hybrid perovskites under varying conditions. Adapted from [64].

440 After observing a strong and coherent carrier–lattice coupling effect in perovskites, a recent study es-
 445 tablished that ultra–fast lattice distortions play a key role in the initial processes associated with charge
 transport [55]. While debate around the nature of charge carriers and the origin of such exceptional PV
 characteristics is still ongoing, some theoretical studies have suggested the potential role of intrinsic ferro-
 450 electricity or bulk PV effects in the effective separation of charges [56, 57]. Other studies focused on the
 effect of surface fields and diffusion [58], carrier-lattice interactions [59–61], and large polaron formation
 [62, 63] to explain perovskite’s unique characteristics. Varying observations and explanations about the
 nature of carrier dynamics and defects in perovskites lead to ambiguity and a clear understanding of carrier
 generation, separation, transport and accumulation is currently lacking. The complexity of these studies
 might be due to an important number parameters such as grain boundaries, phase impurity, compositional
 455 non-uniformity, interfaces and more. Further research is necessary to understand better the exceptional
 characteristics of perovskite solar cells [12].

2.5 Halide perovskite phase stability and scaling challenges

2.5.1 Halide perovskite symmetry and phase effects

455 The archetypal halide perovskite structure involves cubic symmetry and corresponds to a Pm3m space group
 with 12-fold coordination of the A cation, 6-fold coordination of B cations, and corner sharing BX₆ octa-
 460 hedra. Several factors can result in a deviation from cubic symmetry, such as size effects and temperature.
 Analysis of perovskite crystals revealed that in general, perovskites adopt cubic structures and undergo
 phase transitions from cubic to tetragonal to orthorhombic upon temperature reduction [22]. Symmetry of
 perovskites increases with temperature. At room temperature MAPbI₃ forms a tetragonal structure, and
 MAPbCl₃ and MAPbBr₃ form cubic structures. Kanatzidis et al. conducted a detailed study on MA, FA,
 Pb and Sn perovskite combinations and identified three distinct phase transitions: a high temperature α-
 465 phase, an intermediate temperatre β-phase, and a low temperature γ-phase [64]. These are in agreement
 with previous studies conducted by Poglitsch and Weber. Another δ phase can exist, but it is considered as
 non-perovskite as it is hexagonal and does not exhibit PV properties (see Figure 6b). It can be noted that
 FA-based perovskites do not exhibit high temperature phase transformation, which might be interesting for
 their solar cell application. Phase transitions occurring via external temperature or pressure are important
 to be considered during processing and solar cell application as they play an important role in the fabrication
 of efficient and reproducible PSCs.

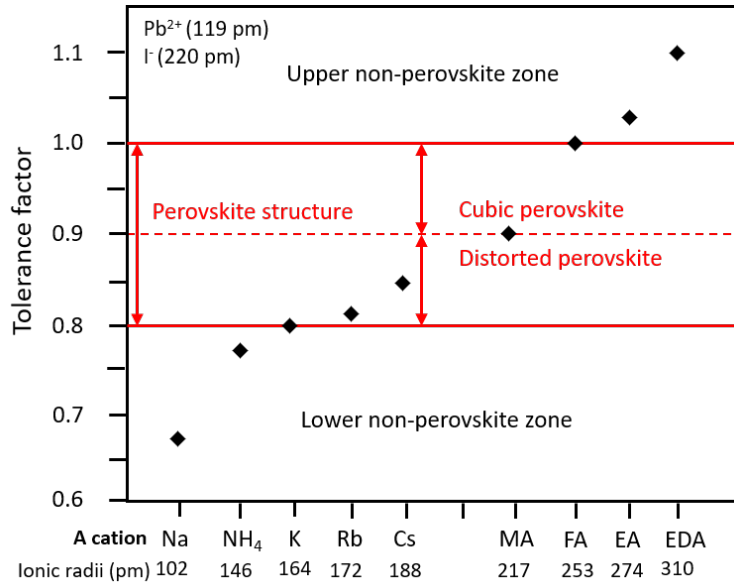


Figure 7: The tolerance factors (τ) for the different cations (A) in the APbI_3 perovskite system. Common cations such as Cs, MA, and FA lead to a τ value in the range of 0.8–1.0, which is indicative of a cubic perovskite phase structure. The ethylammonium (EA) and ethylenediamine (EDA) cations are too big and give tolerance factors >1.0 to fall into the “upper forbidden zone” and thus cannot form the perovskite structure. The group I alkali metal cations (Na, K, Rb) and NH_4 have a τ value <0.8 which falls into the “lower forbidden zone”, and therefore are also unable to form perovskites. (Adapted from [12])

2.5.2 The Goldschmidt tolerance factor

The Goldschmidt tolerance factor (τ) is an empirical index used to predict the formation of different crystal structures of ABX_3 , its value varies depending on the size of ABX_3 ions.

$$\tau = \frac{r_a + r_x}{\sqrt{2}(r_b + r_x)} \quad (6)$$

475 Hexagonal polytypes often occur when the tolerance factor is above 1, which happens due to an increase of the radius of the A cation (r_A), or a decrease of the radius of the B cation (r_B) or X anion (r_X). The electronic properties of perovskite compounds are mainly governed by the B-X bond of the inorganic framework. The size of the A cation can cause distortion of the B-X bond thus adversely affect its symmetry [31, 65].

480 The Goldschmidt tolerance factor is generally used to judge the structural stability of perovskite compounds. The tolerance factors of different APbI_3 systems have been calculated and compared on Figure 7, with A = Na, K, NH_4 , Rb, Cs, MA, FA, EA (ethylamine), and EDA (ethylenediamine). Ideal cubic perovskites are formed when τ is in the range $0.9 < \tau < 1$ and distorted perovskite structures appear when
 485 $0.8 < \tau < 0.9$. For values of τ larger than 1 or smaller than 0.8, the possibility of forming a perovskite diminishes. It can be expected that τ in the middle of the range 0.8–1, and thus away from both non-perovskite zones, would form a stable perovskite [66]. As can be seen on Figure 7, τ is close to 1 for FAPbI_3 , which is therefore prone to formation of a hexagonal and photoinactive δ -phase. For CsPbI_3 , τ is just above 0.8 and it usually crystallizes into a δ -phase. Finally, MAPbI_3 has a τ very close to 0.9, the middle of the
 490 perovskite zone, and forms a photoactive perovskite phase.

Mixing different cations and anions can improve structural stability of perovskites, by bringing the value of τ closer to the middle of the zone. For example, the addition of Cs or MA to FAPbI_3 moves τ value down to stabilise its cubic phase. When properly mixed and/or grown, FAPbI_3 can therefore adopt a cubic unit
 495 cell at room temperature with the FA cations formally disordered over 24 orientations with the perovskitic PbI_3 framework [67].

However, for systems of mixed perovskites, effective τ close to 0.9 is a good guidance for selecting the ions or combination of ions but it is not a sufficient condition on its own for predicting structural stability.

Indeed, at certain concentrations, secondary non-perovskite phases can form [66]. Phase purity also plays a significant role in intrinsic long-term stability of the mixed perovskites as cations with large differences in the ionic sizes between the additives (Na, K, Cs, Rb) and the matrix system (FA/MA mix) are preferred for stabilizing the perovskite structure as long as there is no non-perovskite secondary structure formed. The crystal structure also plays a role in structural stability as cubic structures with higher symmetry show more stability than tetragonal structures even if the cubic structure is a mixed perovskite and the tetragonal one is pure. For example, a tetragonal MAPbI₃ with τ 0.9 is less stable than some mixed cubic perovskites (FA-MA-Cs).

2.5.3 Phase stability challenges

An important challenge for halide perovskites such as CsPbI₃, consists in stabilising its black photoactive phase (α -CsPbI₃) at room temperature. Its calculated tolerance factor being 0.8, the formation of an orthorhombic yellow phase (δ - CsPbI₃) is favored over the cubic black phase which is only stable at temperatures above 310°C [37]. In the α -CsPbI₃ at RT, the size of Cs cations is too small to sustain the PbI₆ polyhedra, thus it readily degrades into orthorhombic δ - CsPbI₃. In order to stabilize α -CsPbI₃, the tolerance factor can be increased by partial substitution of either Cs⁺ ($r = 167\text{pm}$) with bigger cations like FA⁺ ($r = 253\text{pm}$) and MA⁺ ($r = 21\text{pm}$) in the A-site or I⁻ ions ($r = 220\text{pm}$) with smaller anions such as Cl⁻ ($r = 181\text{pm}$) and Br⁻ ($r = 196\text{pm}$) in the X-site. Another solution would be to stabilise the crystal structure with more symmetry by reducing the crystal dimension. That can be achieved with suitable dopants or additives to the precursors of CsPbI₃, which would restrict the dimensions of crystals to a few nanometers thus effectively stabilise the cubic CsPbI₃. Encouraging results have been achieved using these methods and the α -CsPbI₃ has been stabilised at RT in ambient conditions. However, the crystal structure formed at RT was claimed to be orthorhombic, not cubic as the one formed at high temperature [68]. Incorporation of additives such as HI [37], sulfobetaine zwitterion [69], or ethylenediamine (EDA), [70] resulted in a stabilized photoactive phase at RT. When HI is introduced into CsPbI₃, the stabilisation of the black phase at RT is reported by Snaith et al. to be due to the strain created in the crystals. Solar cells of different architectures were built from this HI-induced black phase CsPbI₃ and the best PCE was found to be 2.9% in planar-inverted cells which lasted only a few hours [37]. Lou et al. developed a sequential isopropanol treatment method to improve the PCE to 4.1% in solar cells created using the same HI additive in CsPbI₃ precursor with a stability of a few days. Following that, Kim et al. created a PSC with an inverted architecture which had a PCE of 4.88%. However, size-controlled phase stabilisation using quantum dots, seems much more effective as it raised the PCE beyond 10%, and the stability nearly to a month [71, 72]. Recently, nanocrystal-based devices demonstrated a PCE above 13% [73]. Including a small amount of a 2D perovskite, ethylenediamine lead iodide EDAPbI₄, was also proven to stabilise the α -CsPbI₃ at RT for months with a PCE above 11.5%. α -CsPbI₃ can also be stabilised by partial substitution of Pb²⁺ with Sb³⁺ [74], Ca²⁺ [75], or Bi³⁺ [76], which at optimal concentration could convert all of the δ -CsPbI₃ into α -CsPbI₃ and such a device could bring an efficiency of 13.2% [76].

In general, the formation or stabilisation of black phase at RT is achieved by reduction in crystal or grain size and microstrain in crystals. However, the grains/crystals are confined to nanometer order by both the size of the metal ion and its interactions with other ions acting to control crystallisation and grain growth [77]. Not enough research has been performed on CsPbI₃ perovskites, as the actual methods of stabilisation of the black phase at RT are still unclear, there is also a lack of studies on charge carriers and their dynamics inside CsPbI₃. Moreover, the device structures are not optimised. Degradation mechanisms need to be studied in-depth to stabilise the black phase of CsPbI₃ at RT and in ambient environment for sufficiently long time. Similar issues surround FA and MA based materials, in which several strategies have been used to avoid the formation of the δ phase and improve their phase stability in recent years. These include: tolerance factor adjustment, additive processing, dimensional engineering, interfacial modification, defect passivation, and in situ growth. However, these approaches can only enhance the phase stability to some extent. Their contribution to long-term stability is still unknown [78].

Finally, thermodynamics need to be taken into consideration to assess of the intrinsic stability of a perovskite structure. It has been shown that MAPbX₃ with X = Cl, Br, I, decomposes into PbX_{2(s)}, MA_(g) and HX_(g) and the energy of formation of the products confirms that MAPbI₃ and MAPbBr₃ are thermodynamically more stable than MAPbCl₃ [79]. Intrinsic ion migration occurs under the influence of the electric field

generated in the device during its operation or biased externally in the dark. Such ion migration is believed to affect the long-term stability of perovskite solar cells. Migration of ions must be mediated by defects in any ionic solid. The rate of migration of ions depends on the available interstitial space, Schottky defects (cation or anion vacancies), the size or charge of the ions. Indeed, smaller ions and ions with smaller charge tend to migrate faster than larger ions and ions with greater charge. It is also dependent on the ion jumping distance.

In perovskites, it is believed that ions mainly migrate through cation and anion defects (i.e. vacancies) but the actual migration channel in polycrystalline films is unknown. Grain boundaries are considered as preferred regions of ion migration, thus it is possible to minimize it by reducing the number of grain boundaries. However, it won't totally suppress the process, as halides have also been observed in migration in single crystals of MAPbI₃ [80] and MAPbBr₃ [81]. The activation energy of migration can show how easily an ion migrates in a perovskite film [82, 83]. However, it is not known if ions can migrate if not under bias electric field, and at room temperature.

Characteristics of polycrystalline films can be intrinsic sources of instability too. Thermal strain generated during the annealing process of perovskite films is an example as it accelerates degradation of the perovskite due to the thermal expansion of the substrate and perovskite [84]. The degradation speed largely depends on the amount of strain applied. The nature of the stress applied (tensile or compressive) also influences the stability of the perovskite [85]. Therefore, strain-induced degradation should also be considered for enhancing overall stability of perovskite devices. Stress-induced phase transition, or ferroelasticity, has also been observed in MAPbI₃ perovskites, and generates intragrain strain that can be another important source of instability and needs to be considered for improved long-term stability [86]. Finally, the crystal orientations should also be investigated, as it has been found that moisture corrodes some crystal planes faster than the others [87].

2.5.4 Scaling up challenges

For outdoor installation and commercialisation, perovskite solar cells must guarantee to produce stable power at operating conditions of real sun radiation, under atmospheric moisture and oxygen and raised temperature due to heating for a period of about 25 years. Both intrinsic or structural stability of perovskite and extrinsic stability under different environmental stresses such as light, heat, humidity and oxygen [88] are critically important, and need to be considered. Therefore, strategies to prevent moisture-degradation without much addition to the overall cost are investigated. These include the device encapsulation or material modification by introduction of hydrophobic layers [89, 90], surface passivation [91], or incorporation of 2D perovskite having hydrophobic organic group into 3D perovskites [92].

Performance deterioration and material degradation are also issues that should be solved rapidly [12].

2.6 Polytypism in halide perovskites

Polytypism is a subset of polymorphism in which the crystalline structure is identical along two dimensions but varies in the third. Perovskite polytypes differ in the stacking sequence of the close-packed AX₃ layers. Recently, 3D hexagonal polytypes, reported using the Ramsdell notation, were observed in lead halide perovskites, and their role as intermediates during the crystallization process was discovered [93].

Perovskites derived from the cubic aristotype Pm3̄m adopt a cubic close-packed AX₃ stacking sequence (3C polytype) giving rise to BX₆ corner-sharing octahedra. Hexagonal polytypes commonly occur when the tolerance factor $\tau > 1$ (Eq. 7), which arises due to an increased radius of the A cation (r_A) or a decrease of the radius of the B cation (r_B) or X anion (r_X). These polytypes are generally composed of a combination of hexagonal close-packed and cubic close-packed sequences, resulting in face-sharing BX₆ octahedra. Due to the vast number of stacking possibilities as observed on Figure 8, there is a great amount of potential new structures with different physical properties related to the octahedra connectivity, such as the band structure. The observed polytypes and crystal phases largely depend on the growth method and conditions chosen. In their EDX analysis and single-crystal structure refinements, Gratia et al. revealed the uptake of both I and Br in the 4H and 6H polytypes as well as the DMSO intermediate. On the contrary, the

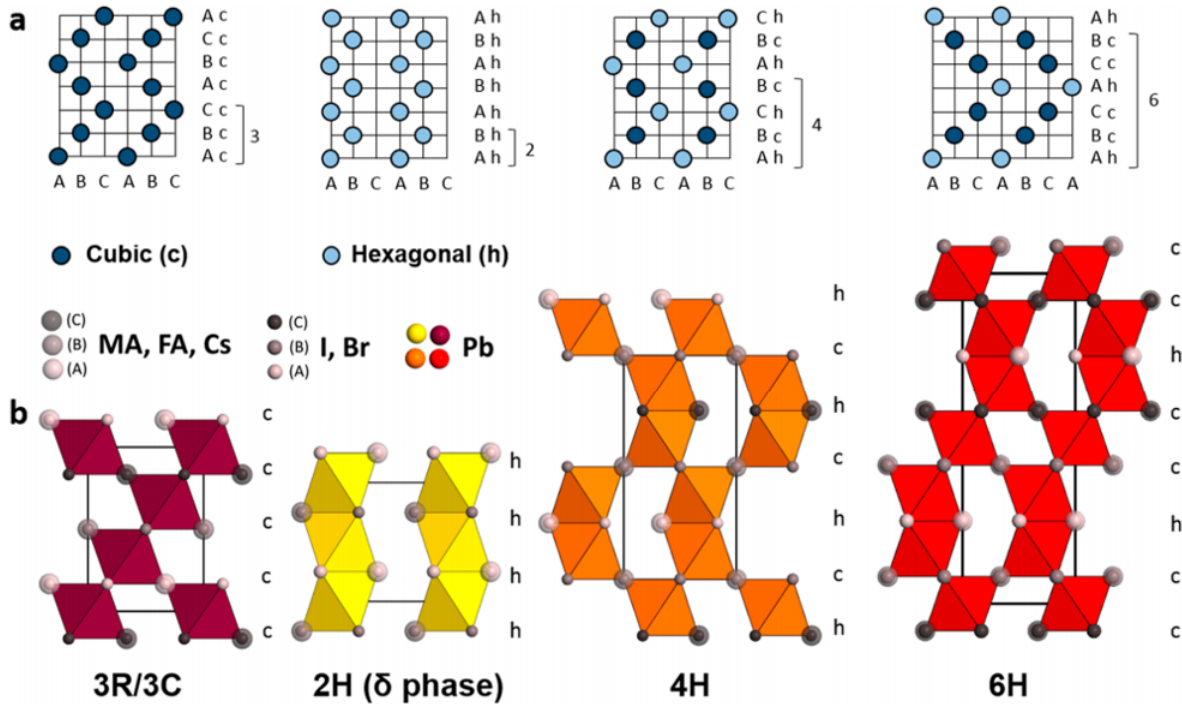


Figure 8: a) The AX₃ stacking sequences of hexagonal lead halide perovskite polytypes (2H (“delta phase”), 4H, 6H), and cubic (3C)/rhombohedral (3R) perovskite phases. h: hexagonal close-packed: light blue circles; c: cubic close-packed: dark blue circles. b) Corresponding representation of the refined single-crystal structure viewed along a. A 1D framework (2H) is favoured by face-sharing, whereas corner-sharing (3C/3R) or a linear combination of corner- and face-sharing octahedra lead to a 3D framework (4H, 6H). (Reprinted from [93]).

2H phase, does not take up any Br even when grown from bromine-containing precursor solutions. The compositional dependency of unit cell volume revealed that the 3C and 6H structures are mixed ion compositions confirming the EDX data. On the opposite, 2H is a pure iodide phase. The structural data collected on 2H, 4H, 6H, and 3C single crystals confirmed these observations. The space group symmetry in both the 4H and 6H polytypes, generates two crystallographically distinct anion positions related to face and corner sharing of octahedra. The heavier iodide anion in the hexagonal perovskite polytypes 4H and 6H preferentially occupies the face-sharing position. Thus the Br⁻ <-> I⁻ exchange must trigger the crystallization sequence in the 2H phase. This breaks up the face-sharing connectivity of the 2H phase, and the initial anion exchange drives the polytypic transformations [93]. In the same study, it was also shown that doping of 1% Cs yields 6H and 2H/4H phases which proportion decreases with an increase of the Cs doping. The group concluded that the crystallization scheme of mixed ion perovskites takes the following steps. A Br⁻ containing precursor matrix diffuses at 100°C in the presence of DMF/DMSO, into the 2H phase, which leads to a Br-I, and probably also MA-FA, exchange reaction. This produces the 3D hexagonal iodide/bromide-containing polytype 4H. Next, 4H gradually transforms into 6H and 3R/3C by continuous exchange reactions. A competition between DMSO intermediate crystallization and bromide (+MA) uptake from 2H takes place at room temperature. Following the crystallization of the DMSO intermediate, high temperatures (above 150°C) are required to proceed to solid-state exchange reactions which convert the hexagonal phases further to 3C/3R. A film degradation takes place as these temperatures are close to the thermal stability of black perovskite in the film. This degradation manifests itself by the appearance and increasing phase fraction of PbI₂. The hypothesis made was that the driving force for the H-4H-6H-3R(3C) crystallization sequence is an increase of Madelung energy as the stacking of AX₃ layers goes from pure hexagonal (2H) to a cubic/hexagonal ratio of 1:1 (4H), 2:1 (6H), and eventually pure cubic (3C). Indeed, repulsion of B cations between face-sharing octahedra results in a loss of Madelung energy. The Madelung energy is another name for the electrostatic energy, it represents the sum of Coulomb potentials and is often determined using the Ewald method. Hexagonal over cubic stacking is stabilized due to BB bonding, BX covalency, and B-site vacancies which compensate for the energy loss. [93]

The colour of the hexagonal phases is related to the band gap variations that depend on the connectivity of the PbI₆ octahedra. It has also been reported by Kamminga et al. that an increase in connectivity from

635 corner-, via edge-, to face-sharing results in an increase in the band gap [93, 94]. Both cubic and hexagonal
phases are observed experimentally [93]. Recently, single-crystal structures obtained from crystals grown by
liquid-liquid diffusion of the mixed ion perovskite precursor solution revealed the formation of the polytypic
structures 4H and 6H. These were found to dominate the phase composition in the unannealed perovskite
640 films. It also appeared that these polytypes play a crucial role between the precursor film and the final
black phase with new complex sequences observed. The stability of these phases is composition-dependent,
the formation of hexagonal phases can be inhibited by a low substitution of Cs⁺ cations, thus rationalising
the widely reported superior stability and reproducibility of mixed PSCs containing Cs [93].

For a successful commercialisation, the high power conversion efficiency observed on small area lab per-
645 ovskite solar cells needs to be translated to larger area cells. Unfortunately, a performance drop is observed
when scaling up. It can be attributed to different factors such as an increase in sheet/series resistance, loss
in active area due to carrier collection or decrease in homogeneity over large areas.

The substantial gap between the performance of small-area and large-area modules, could be limited by
650 optimizing the design of large-area cells that limit the output power significantly. Modeling of structure of
an optimised design of the front electrode with metal grid can result in a similar PCE that smaller-area cells
in modules of dimensions 156 mm × 156 mm. Another important reason for this performance gap comes
from the difference in morphology and quality of larger films. These are made by spin-coating and scale-up
methods, such as balding or slot-die coating. Many methods used for small-scale fabrication in laboratories,
655 are not suited for large-scale solar cells. Recently the resulting efficiency difference has been narrowed by
the formulation of new methods adapted to scaled-up cells such as ink jet printing and modification of
annealing/drying conditions specific to the scale up methods. Structurally, the scaling up efficiency drop
is partially due to polytypism, as more different polytypes are present on larger solar cell areas, resulting
in a probable transition to the non-photoactive yellow phase. In order to reduce this efficiency drop during
660 scaling up, polytypism needs to be further studied to investigate different polytypes and assess their total
energies and electronic impact.

2.7 Summary

With a rapid increase in efficiency and cost effectiveness, PV energies contribute more and more to the
transition to renewable energies, which aim is to entirely replace fossil fuels. Currently, metal halide per-
665 ovskites are the most promising materials for PV applications, with record efficiencies exceeding 24% power
conversion. Hybride organic-inorganic halide perovskites represent the highest efficiencies, however they are
less stable than all-inorganic halide perovskites. In both cases, the stability of the material causes issues,
especially during the scaling up process when phase changes take place. The archetypal halide perovskite
structure involves cubic symmetry. However, several factors can result in a deviation from the cubic sym-
670 metry, such as size effects, composition and temperature. Upon temperature reduction halide perovskites
can undergo a phase transition from cubic to tetragonal to orthorombic structure. A hexagonal phase (also
called δ phase, or yellow phase) can also appear, and does not exhibit PV properties. An important challenge
for halide perovskites consists in stabilising at room temperature its photoactive phase, also called the black
phase, and impede the transformation to yellow phase that happens at lower temperatures. Non-uniformity
675 of halide perovskites results in a quick drop in the device efficiency when scaled up. Polytypism represents
one of the main obstacles due to the presence of face sharing octahedra inhibiting good PV properties.
Polytypism is a subset of polymorphism, in which crystalline structure is identical along two dimensions but
varies in the third. Perovskite polytypes vary in their stacking sequence. The 3C polytype represents the
PV active black phase, and favors corner-sharing. The black phase can be found in the 2H polytype, which
680 favors face-sharing. Many combinations of corner and face sharing polytypes exist and their phase stability
at room temperature is being studied.

3 Methods

The aim of this computational project was to develop a perovskite polytype builder that gives the energies and probability of formation of different polytypes. The methodology followed can therefore be divided into two sections: creation of the perovskite polytype builder and energy calculations associated with boltzmann population distribution.

3.1 Creation of the perovskite polytype builder

In order to develop the code that would form our perovskite polytype builder, the Atomic Simulation Environment (ASE) library was originally used. It is a set of tools and Python modules for setting up, manipulating, running, visualizing, and analyzing atomistic simulations.

The first step was to read the primitive POSCAR file provided giving the primitive structure of the CsPbI₃ unit cell. To form the unit cell, the missing I and Cs atoms were added and combined with the previous structure. The structure was rotated to be visible along the (111) plane like in the paper by Gratia et al. [93]. Therefore, two rotations had to be performed, one along the x direction by 45° and one along the z direction by 90-tan(√2)°. Two opposite orientations were then picked as building blocks A and B. By combining and translating these building blocks, the polytypes 3C, 2H, 4H, 6H and 12H were created. The unit cell borders automatically defined by ASE had to be modified and the duplicate atoms deleted. The code and the different steps used to check it are visible in the Appendix. POSCAR files containing the polytype structures were generated and visualised using VESTA.

The terms 3C, 4H, 6H and 12H refer to the Ramsdell notation used for describing halide and oxide perovskite polytypes [95]. Consequently, Gratia et al. decided to use the term 2H to refer to the δ phase in lead halide perovskites [93] and the notation was kept in this study. The table below compares the different notations and the symmetry characterizing the phases as obtained from single-crystal growth.

Table 1: Comparison of the different notations, stacking sequences and unit cells parameters between the hexagonal polytypes (2H, 4H, 6H) and the Rhombohedral/Cubic Perovskite (3R, 3C) phases. (reprinted from [93]).

Ramsdell notation	ABC	h-c notation	a [Å]	c [Å]	volume [Å ³]	crystal system	space group
2H	AB	h	8.66	7.9	513	hexagonal	P6 ₃ /mmc
3R	ABC	c	8.85	11.23	761	rhombohedral	R $\bar{3}$
3C	ABC	c	6.31	6.31	251	cubic	Pm- $\bar{3}$ m
4H	ABCB	hc	8.81	15.2	1023	hexagonal	P6 ₃ /mmc
6H	ABCACB	hcc	8.84	22.45	1520	hexagonal	P6 ₃ /mmc

3.2 Electrostatic energy calculations

The effect of charge interactions was studied in the different perovskite structures previously built. In order to measure that, the electrostatic potential energy of the system of charges was calculated. A pair of charges will always have some potential energy because, when released from rest, they will either move away from (if the charges are the same) or towards (if the charges are different) each other. The electrostatic potential energy that we are comparing for different structures is specifically the energy associated with a set of charges arranged in a certain configuration. The potential energy (U_e) depends on the amount of charge that each object contains (q), how far apart the charges are (r), and Coulomb's constant (k):

$$U_e = k \frac{q_1 q_2}{r} \quad (7)$$

Considering a main cell consisting of N particles with charges q_i at position r_i in a cubic box of length L , and surrounded by replica cells that fill the whole cell, the energy U associated to the main cell in this periodic boundary conditions system is:

$$U = \frac{1}{4\pi\epsilon} \frac{1}{2} \sum_{i=1}^N \sum_{j=1}^N \sum_{\mathbf{n} \in \mathbb{Z}^3} \frac{q_i q_j}{|\mathbf{r}_{ij} + \mathbf{n}L|} \quad (8)$$

Where $\mathbf{r}_{ij} = \mathbf{r}_i - \mathbf{r}_j$. The sum over \mathbf{n} is over all simple cubic lattice points, $\mathbf{n} = (n_x L, n_y L, n_z L)$ with n_x , n_y and n_z integers. The † indicates that the $i = j$ term must be omitted for $\mathbf{n} = 0$ to avoid to take into account the interaction of a particle with itself.

The energy U is due to the Coulomb interaction of the particles located inside the main cell with other particles present in the cell, as well as with the particles located in the replica cells.

Different electrostatic energy calculations are possible, the direct summation being one of them. However that method is excessively computationally demanding. In Eq. 8, the sum over \mathbf{n} is an infinite series because it runs over all \mathbb{Z} . Therefore, in order to numerically evaluate the sum, a cut-off must be performed, assuming that contributions arising from larger \mathbf{n} values can be neglected and only values that satisfy $|\mathbf{n}| < n_{cut}$ are taken into account. This is called a spherical sum. There will thus be an error when we compute equation 8 numerically. In theory, the introduction of a cut-off is not a problem as there is no need for an infinitely accurate result. However, in practice, the direct sum method requires a large cut-off to get results accurate enough to be used in simulations. When we increase n_{cut} , we get a more accurate value of U but the number of cells to take into account scales as n_{cut}^3 and not linearly because \mathbf{n} is a 3D vector. If we assume that the time needed to compute the sum is proportional to the square of the number of particles we have in the extended system (main cell + replicated cells), then the computer time we need scales as $n_{cut}^6 N^2$, where N is the number of particles in the main cell box. Therefore, despite being a very useful tool to test the correctness of more advanced methods, the direct sum method is of little use for simulations [96]. For this reason, the Ewald summation was chosen in this project.

The Ewald sum is a faster method to compute electrostatic quantities such as energies or forces [97]. It is based on splitting the slowly convergent Eq. n 8 into two series which can be computed much faster and at a fixed level of accuracy [96]. In order to do that, the interaction $1/r$ is splitted as follows:

$$\frac{1}{r} = \frac{f(r)}{r} - \frac{1-f(r)}{r} \quad (9)$$

Where $f(x) = \text{erfc}(\alpha r)$, where α is the Ewald splitting parameter, resulting in the Ewald formula:

$$U = U^r + U^k + U^{self} + U^{dipolar} \quad (10)$$

Where U^r is the real space contribution, U^k is the reciprocal space contribution, U^{self} accounts for the self-energy, and $U^{dipolar}$ represents the dipolar correction. When a spherical sum is performed, these contributions are given by:

$$U^r = \frac{1}{2} \sum_i^N \sum_j^N \sum_{\mathbf{n} \in \mathbb{Z}^3} q_i q_j \frac{\text{erfc}(\alpha)|\mathbf{r}_{ij} + \mathbf{n}L|}{|\mathbf{r}_{ij} + \mathbf{n}L|} \quad (11)$$

$$U^k = \frac{1}{2L^3} \sum_{\mathbf{k} \in \mathbb{K}^3, \mathbf{k} \neq 0} \frac{4\pi}{k^2} \exp\left(\frac{-k^2}{4\alpha^2}\right) \sum_i^N \sum_j^N q_i q_j \exp(-i\mathbf{k} \cdot \mathbf{r}_{ij}) \quad (12)$$

$$U^{self} = \frac{-\alpha}{\sqrt{\pi}} \sum_i^N q_i^2 \quad (13)$$

$$U^{dipolar} = \frac{2\pi}{(1 + 2\epsilon')L^3} \left(\sum_j^N q_i r_i \right)^2 \quad (14)$$

Where ϵ' is the dielectric constant, and $\mathbb{K} = 2 \pi \mathbf{n}/L : \mathbf{n} \in \mathbb{K}^3$. In practice, the sums for U^r and U^k are evaluated performing cutoffs given by r_{cut} and k_{cut} .

The electrostatic energy calculations were performed at room temperature (298K) using the Ewald method on the structures previously constructed. The code can be found in the Appendix.

3.3 Equilibrium distribution

Using the electrostatic energies calculated for different polytypes, the Boltzmann Population Distribution for the different polytypes was calculated for different temperatures and its variation observed. The Boltzmann population distribution is a probability distribution that gives the probability of a certain phase as a function of that phase's energy and the temperature of the system to which the distribution is applied. It is given as:

$$P_i = \frac{1}{Z} \exp\left(\frac{-\epsilon_i}{kT}\right) \quad (15)$$

Where p_i is the probability of state i , ϵ_i the energy of state i , k the Boltzmann constant, T the temperature of the system and Z is canonical partition function:

$$Z = \sum_i^M \exp\left(\frac{-\epsilon_i}{kT}\right) \quad (16)$$

With M the number of all states accessible to the system of interest.

The Boltzmann distribution is the distribution that maximizes the entropy and can therefore show the most stable phase as isolated systems spontaneously evolve towards the maximum entropy phase, which is their thermodynamic equilibrium. That can be explained by the second law of thermodynamics, which states that entropy of an isolated system never decreases over time.

In statistical mechanics, entropy is an extensive property of a thermodynamic system. It is closely related to the number of microstates, or microscopic configurations Ω , consistent with the macroscopic quantities that characterize the system such as its pressure, temperature and volume. Assuming that each microstate is equally probable, the entropy, S , is defined as:

$$S = k_B \ln \Omega \quad (17)$$

As entropy is determined by the number of random microstates, it is related to the amount of additional information needed to specify the exact physical state of a system, given its macroscopic specification. For this reason, entropy can be considered as an expression of the disorder, or randomness of a system.

4 Results and Discussion

4.1 Structure models and ranking for CsPbI₃

The structure models for the CsPbI₃ polytypes are visible on Figure 9. Comparing the 3C, 2H, 4H and 6H polytypes generated with Figure 8, shows that the code is functioning as expected generating the structures

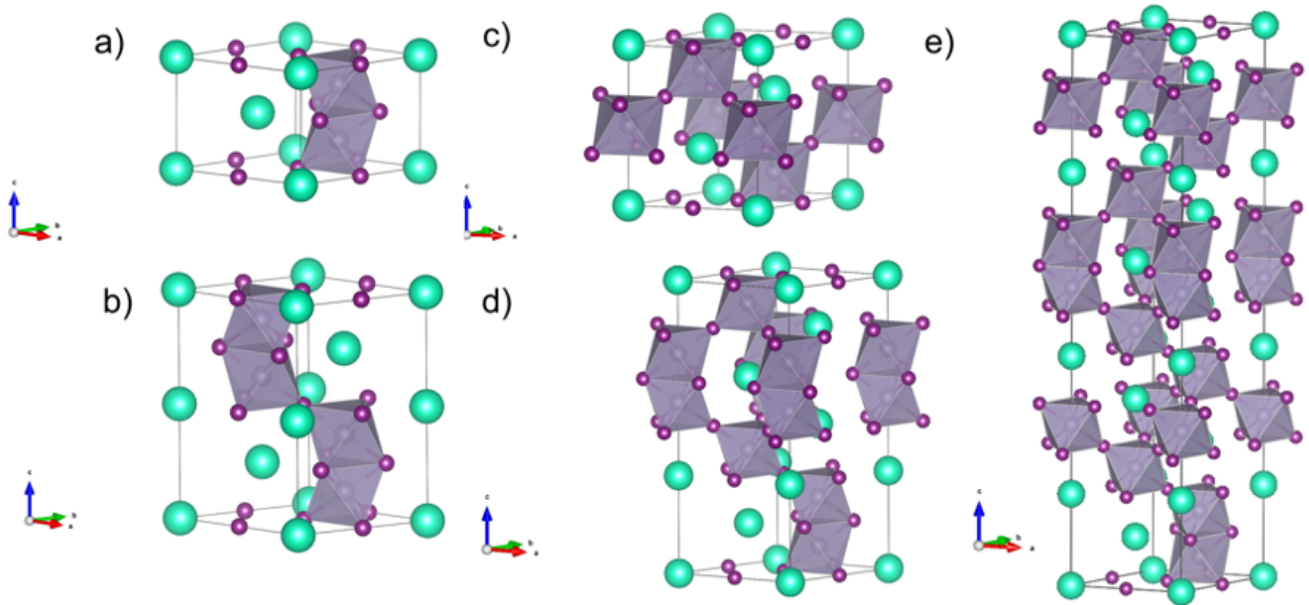


Figure 9: Structure models visualised on VESTA and built for different CsPbI_3 polytypes with a) the 2H polytype, b) the 4H polytype, c) the 3C polytype, d) the 6H polytype and e) the 12H polytype.

discovered and described by P.Gratia et al. in 2017 [93]. It can therefore be used to model structures that have not been observed experimentally yet such as the 12H polytype. How likely these structures are to actually exist has been assessed from their electrostatic energies below.

Calculating the electrostatic energies for different polytypes in CsPbI_3 , resulted in a ladder-like, normalised ranking of electrostatic energy levels for different polytypes visible in Figure 10 a). It appears that the lowest electrostatic energy is present in the cubic/3C polytype, followed by the 12H, the 6H, the 4H and finally, after a larger gap, the 2H.

This is in accordance with the Boltzmann Population Distribution, which shows that at room temperature the cubic or 3C polytype dominates, and its probability of formation decreases with temperature. The probability of formation of the other polytypes also follows the energy ranking, with a decreasing Boltzmann Distribution as the relative energy increases. This was expected as the most stable combinations are the ones with the lowest energy. However, the Population Distribution of these other polytypes increases with temperature. The rates of increase are different as they depend on the relative energy of each structure. The Boltzmann population distribution tells us what structure we would expect for a given temperature, and its probability of existence. For example, as seen in Figure 12, at 300K for SrTiO_3 , almost 100% cubic is expected and none of the others. The rate of increase for the non-cubic structures here, is just due to the energy difference since higher temperatures enable accessing higher energy structures.

Interestingly, these results are very different to what has been observed experimentally, where generally at room temperature, the most stable phase is the yellow one and the black phase can be obtained by heating the perovskite [93]. Here the results are nearly opposite, with the most stable phase being the black one with a probability that decays with temperature.

4.2 Comparison to oxide perovskites

The electrostatic energies have been calculated for oxide perovskites SrTiO_3 , LaCoO_3 and KTaO_3 which represent the most common valencies in halide perovskites. The electrostatic energy level ladders and corresponding Boltzmann Population Distributions are visible in Figures 11, 12, and 13. All the perovskites studied, both halide and oxide, present the same order in the ranking of polytype relative energies. Similarly the same ranking of Boltzmann Population Distributions is conserved. However, the relative energies and the relative energy gaps are different due to a change in valency. The rate of change of the Boltzmann Population Distributions with temperature is affected as well. In the oxides, this rate of change seems to be smaller, with the cubic phase largely dominating for higher temperatures. Again, these results are surprising

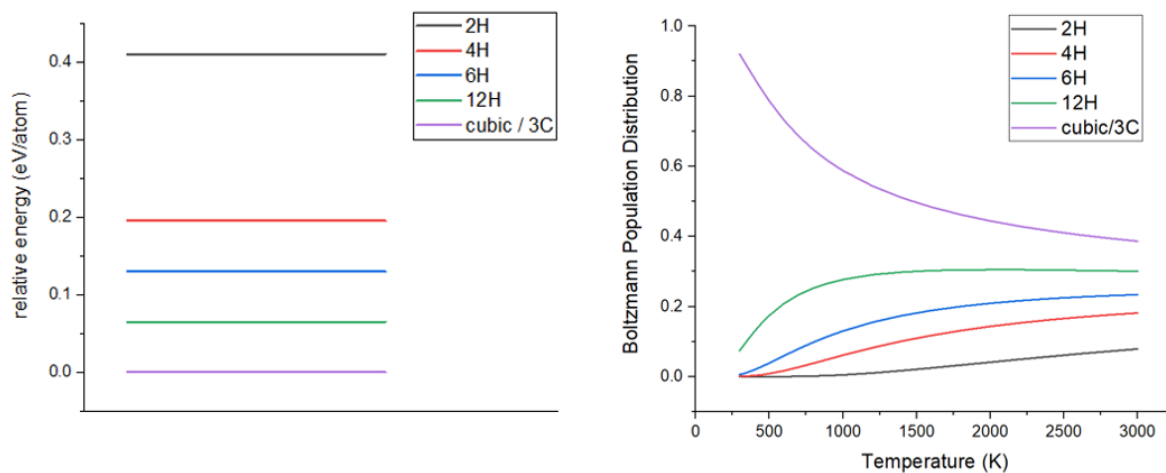


Figure 10: (a) Electrostatic energy level ladder for different polytypes of CsPbI₃. (b) Variation in the Boltzmann Population distribution for different CsPbI₃ polytypes with the temperature.

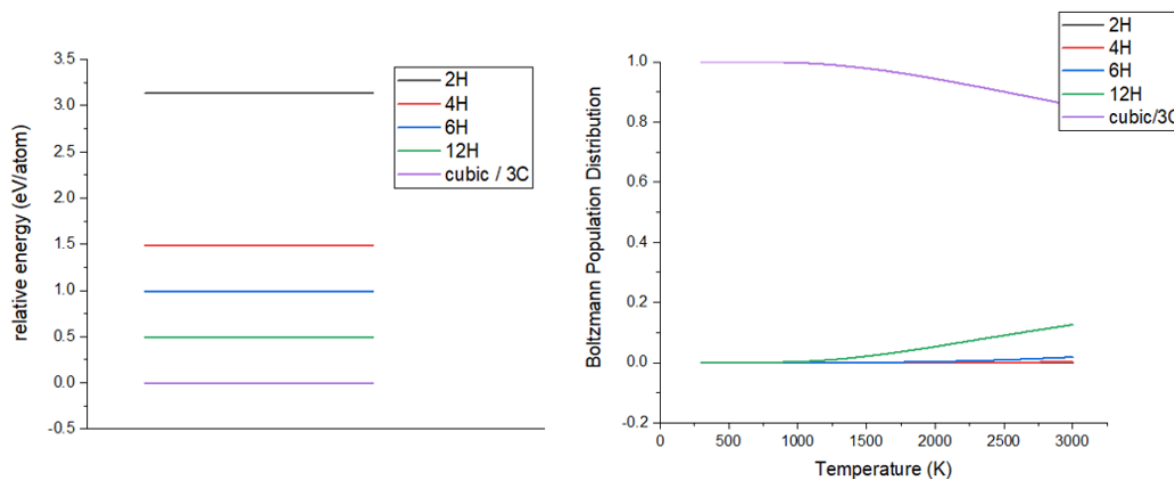


Figure 11: (a) Electrostatic energy level ladder for different polytypes of KTaO₃. (b) Variation in the Boltzmann Population distribution for different KTaO₃ polytypes with the temperature.

and differ from experimental observations probably due to the limitations of the model that will be discussed later on.

4.3 Application to double perovskites

825 The same calculations were applied to the double perovskite Cs₂Pb₂I₆. Again, the order is conserved. However, there is an important difference in the Boltzmann Population Distribution, as for temperatures ranging from 298 to 3000K the cubic phase is largely dominant. The variation with temperature is significantly lower. At very high temperatures the 12H phase goes up to 0.2 but the other phases are negligible. The 2H phase has been omitted from Figure 14b) for clarity the probability was consistently low. However, for better understanding, it is still in the legend for that graph.

830 4.4 Discussion of the model limitations

The discrepancies between this model and the experimental results obtained from literature are due to the limitations of this model, which was very simplified as it only took the electrostatic energy into consideration. The free energy of a material is a balance of the enthalpy and the entropy. Non-equilibrium thermodynamic processes such as defects or excited states, should also be thoroughly considered for more accurate results. 835 This model only considered enthalpy. In many studies of packing in molecular crystals, the free energy is approximated by the static lattice energy, neglecting the contribution from other types of entropy. This may be justified in some cases, however the importance of vibrational entropy has been highlighted by recent studies.

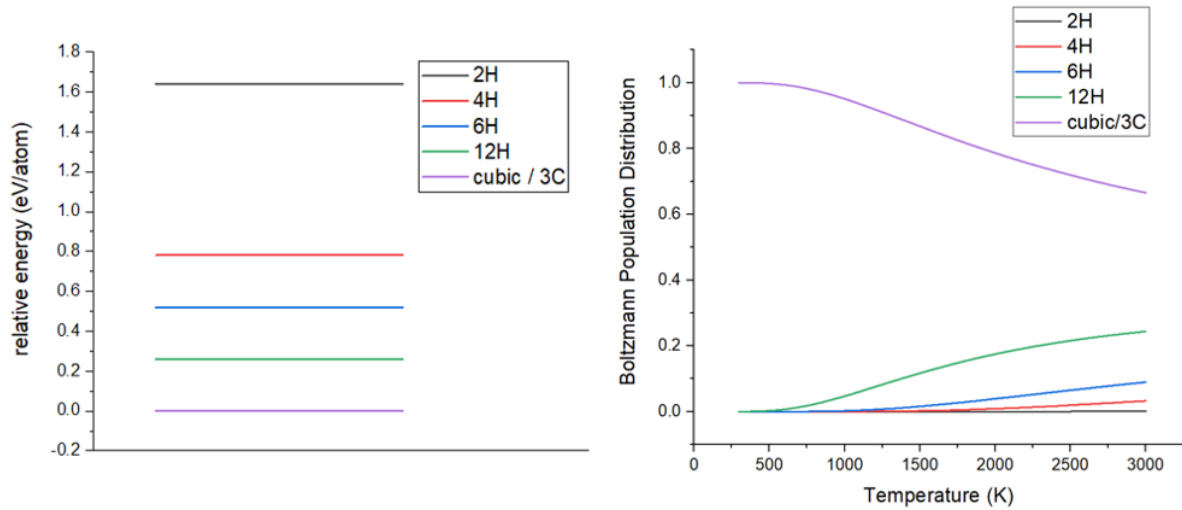


Figure 12: (a) Electrostatic energy level ladder for different polytypes of SrTiO₃. (b) Variation in the Boltzmann Population distribution for different SrTiO₃ polytypes with the temperature.

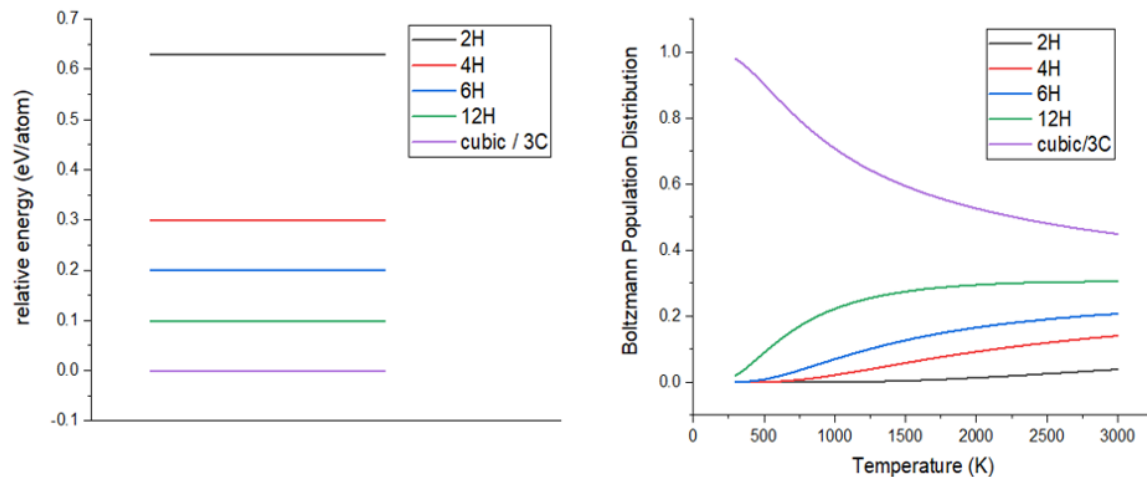


Figure 13: (a) Electrostatic energy level ladder for different polytypes of LaCoO₃. (b) Variation in the Boltzmann Population distribution for different LaCoO₃ polytypes with the temperature.

Entropy of a perfect crystal is zero at 0K. For inorganic materials, engineering entropy is closely related to defect chemistry and site disorder [98]. The minimum in Gibbs free energy of a system comes from a delicate balance between enthalpy and entropy at finite temperatures, which drives the formation of intrinsic defects [99].

The balance between ordered and disordered mixed valance systems across temperature ranges can be determined by configurational entropy [100]. On the other hand, vibrational entropy is closely related to the chemical bond organisation. In general, a high contribution from (vibrational) entropy is suppressed in rigid inorganic lattices where high bond strengths are present. The role of vibrational entropy is therefore enhanced in Zintl compounds or inorganic clathrate where loosely bound (molecular) moieties exist. Entropy also plays a major role in temperature dependent phenomena [99].

In this case, the system is clearly governed by entropy as experimentally, the yellow phase is the most stable (and thus has the highest entropy), whereas the computational results from this model indicate that the most stable phase is the black one, which usually is obtained by heating to increase the entropy. It is clear that entropy plays an important role in the phase definition of these polymorphs and therefore has to be taken into account. There are three main types of entropy not considered in this study: (i) vibrational entropy, (ii) rotational entropy and (iii) configurational entropy [99].

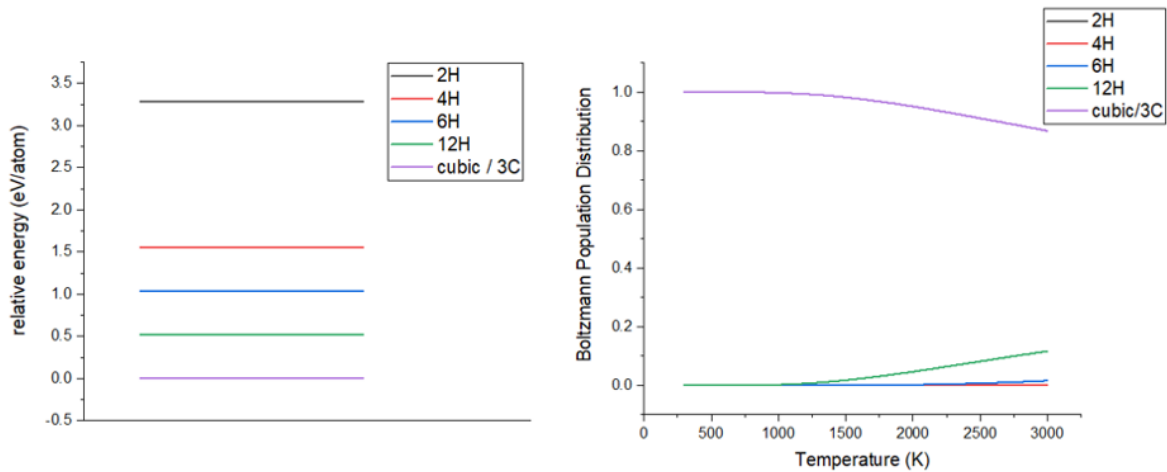


Figure 14: (a) Electrostatic energy level ladder for different polytypes of $\text{Cs}_2\text{Pb}_2\text{I}_6$. (b) Variation in the Boltzmann Population distribution for different $\text{Cs}_2\text{Pb}_2\text{I}_6$ polytypes with the temperature.

- **Vibrational entropy** is computationally accessible via lattice dynamics calculations. The system is treated as a coupled harmonic oscillator to calculate the dynamic matrix (\mathbf{D}) which is obtained from the Hessian matrix. The Hessian contains the second derivatives of the energy with respect to the geometry of the system, obtained directly from density functional theory (DFT) calculations. A set of eigenvectors (phonon modes) and eigenvalues (phonon frequencies, ω) is obtained by solving \mathbf{D} . The vibrational entropy of the system can be obtained from:

$$S_{vib} = -k_B \sum_{q,s} \frac{h}{2\pi} \omega(q,s) + \frac{1}{T} \sum_{q,s} \frac{h\omega(q,s)}{2\pi \exp(-h\omega(q,s)/2\pi k_B T) - 1} \quad (18)$$

With k_B the Boltzmann constant, h the Planck constant, T the absolute temperature and $\omega(q,s)$ the phonon frequencies. These calculations may be expensive due to the fact that populating the Hessian requires many calculations to determine the forces on each ion. It is also necessary to use supercell expansions of the unit cell to ensure that all important elements of the Hessian are accounted for.

Entropy plays a key role in determining which crystal polymorph is energetically favourable in hybrid formate systems as has been shown in recent studies using DFT-based lattice dynamics to calculate the vibrational entropies of these systems [101]. Although the crystal vibrational contributions are expensive to calculate, the importance of such effects cannot be ignored particularly in hybrid materials that exhibit soft phonon modes. These phonon modes are thermally accessible and emerge from weak interactions such as hydrogen bonds. Vibrational effects can also be explored using molecular dynamics [102] which is a computationally costly method but with results which transcend the (quasi-)harmonic approximation made in lattice dynamics techniques

- **Rotational entropy** is only a concern in solid-state sciences due to the spherical symmetry of constituent building blocks, ions. Therefore, the study of its contributions in the solid-state are less developed and when rotational entropy is considered, it is generally in the form of the addition of an analytical term to the energy after a total energy calculation. The analytical expression for rotational entropy of a molecular unit is:

$$S_{rot} = R \ln \left[\frac{\pi^{\frac{1}{2}}}{\sigma} \prod_{j=1}^3 \left(\frac{8\pi^2 I_j k_B T}{h^2} \right)^{\frac{1}{2}} \right] \quad (19)$$

Where I_j are the principle moments of inertia of the molecule and σ is the symmetry number.

However, in this study only inorganic perovskites with centrosymmetric spherical ions at the A-site are considered, thus the rotational entropy is not present, and should not be taken into consideration.

- **Configurational entropy** represents disorder in the nature of site occupancy on crystal sub-lattices, including defects. Standard simulation techniques employ periodic boundary conditions, where a repeating unit is used to build an infinite representation of the system which makes the explicit treatment of configurational disorder challenging, as there will always be a degree of periodicity in the system. In theory, choosing a large enough starting unit could account for disorder, however in practice the size of the unit is constrained by computational demands. The way around these issues is to use statistical thermodynamics methodologies to consider the entropies of ensemble of configurations. All these methods start from the idea entropy of mixing:

$$S_{mix} = -nR(x_1 \ln x_1 + x_2 \ln x_2) \quad (20)$$

Where n is the number of particles and x_n are the fractions of each component. The ideal entropy of mixing assume no interactions between particles. The effects on interatomic forces are then added using a variety of techniques with the most widely applied of these methods being the coherent potential approximation [103] methods, the special quasi-random structure approach [104] (SQS) and the cluster expansion method [105] (CE). These methods have been used extensively to study the effects of disorder in solid-state systems [99]. In hybrid systems, the understanding of configurational order/disorder relationships is critical in many cases. In particular, in lead-based hybrid halide perovskites with the general formula $APbX_3$, mixing organic cations on the A-site with halides on the X-site can result in the creation of some of the most efficient solar cells.

Entropy has an undoubtedly important impact on the crystal chemistry of hybrid inorganic-organic materials. In most cases where the entropy is considered in solid state systems, only one of the three types discussed above is considered. However, in some defect dependent cases such as organic-inorganic perovskites, a combination of configurational disorder together with vibrational entropy account for the material's properties. In these hybrid materials, long organic linkers and porous materials lead to high vibrational entropies, while, at the same time, substitutional defects seem to be relatively easy to introduce. The important role of both vibrational [106] and configurational [107] entropies has been emphasized computationally in these materials. However, more research is needed in order to fully understand and quantify the role of entropy in fully inorganic halide perovskites.

Table 2: Summary of the types of entropy not considered in this study, their related properties and how they can be accounted for computationally (reprinted from [99]).

Entropy	Properties	Calculation
Configurational	Bandgap; magnetic ordering; thermal conductivity; phase stability; electronic polarisation	Cluster expansion; special quasirandom structures; small set of ordered structures; lattice Monte Carlo
Rotational	Phase stability; thermal conductivity; electrical polarisation	Molecular dynamics; nudged elastic bands
Vibrational	Bandgap; phase stability; thermal conductivity; vibrational spectra	Lattice dynamics; molecular dynamics

5 Conclusions (and suggestions for further work)

At present, while a perovskite cell efficiency of above 20% is being achieved by most leading laboratories in lab-scale devices, long-term stability, scalability and toxicity of Pb are obstacles to commercialisation. This

project studied one of the phenomena that impedes the scalability of perovskite cells, the transition from the photoactive, black (corner-sharing 3R/3C) phase to the non-photoactive yellow (face-sharing) phase. One of the challenges facing perovskite solar cells is therefore the stabilisation of their black phase at room temperature. In this project, the energies and stability of different polytypes was studied. More specifically, the aim of this project was to model 3D structures of different perovskite polytypes and calculate their electrostatic energies using the Ewald Method.

The electrostatic energy level ladders built for one halide perovskite (i.e CsPbI₃), three oxide perovskites (i.e SrTiO₃, LaCoO₃ and KTaO₃), and a double perovskite, presented relative energies normalised around the lowest present in the cubic phase. These relative energies increased following the order: 3C, 12H, 6H, 4H and finally 2H. The Boltzmann Population Distribution decayed with temperature for the 3C polytype and increasing for all the others. These results differ from those observed experimentally and found in literature due to the limitations of this model which only considers the electrostatic energy and ignores the contribution of other significant parameters such as vibrational and configurational entropy.

To continue this work an improvement of the model built is necessary, taking more parameters into account. More accurate energy descriptions could also be achieved by going beyond electrostatics and applying methods such as density function theory (DFT) on the polytypes built. Finally, it would be interesting to integrate the perovskite building code with the energy calculations building a software that could model any polytype and give its associated energies and characteristics, saving a lot of time to experimentalists.

References

- ¹S. Bilgen, S. Keleş, A. Kaygusuz, A. Sarı, and K. Kaygusuz, “Global warming and renewable energy sources for sustainable development: A case study in Turkey”, *Renewable and Sustainable Energy Reviews* **12**, 372–396 (2008).
- ²“Global, Regional, and National Fossil-Fuel CO₂ Emissions”, Carbon Dioxide Information Analysis Center (2017).
- ³M. Da Graca Carvalho and N. H. Afgan, *2004 New and renewable energy technologies for sustainable development* (World Scientific Publishing Co., Jan. 2007), pp. 1–370.
- ⁴T. Soga, *Nanostructured Materials for Solar Energy Conversion* (Elsevier, 2006).
- ⁵C.B.Honsberg and S.G.Bowden, *Photovoltaics Education Website*, 2019.
- ⁶J. Nelson, *The Physics of Solar Cells* (Imperial College Press, May 2003).
- ⁷*Solar cells and power, Part 1 – basic operation - Power Electronic Tips*.
- ⁸“Novel Up-Conversion Concentrating Photovoltaic Concepts”, PhD thesis (Heriot-Watt University, 2015), p. 193.
- ⁹W. Shockley, H. J. Queisser, and R. Ell, “Detailed Balance Limit of Efficiency of pn Junction Solar Cells”, *Journal of Applied Physics* **32**, 510 (1961).
- ¹⁰S. Rühle, “Tabulated values of the Shockley-Queisser limit for single junction solar cells”, *Solar Energy* **130**, 139–147 (2016).
- ¹¹I. Renewable Energy Agency, *Renewable power generation costs in 2017: Key findings and executive summary*, tech. rep. ().
- ¹²A. K. Jena, A. Kulkarni, and T. Miyasaka, “Halide Perovskite Photovoltaics: Background, Status, and Future Prospects”, *Chemical Reviews* **119**, 3036–3103 (2019).
- ¹³M. A. Green, A. Ho-Baillie, and H. J. Snaith, *The emergence of perovskite solar cells*, 2014.
- ¹⁴I. Renewable Energy Agency, *Renewable Energy Technologies: Cost analysis series*, tech. rep. (2012).
- ¹⁵A. Khatibi, F. Razi Astarai, and M. H. Ahmadi, *Generation and combination of the solar cells: A current model review*, Apr. 2019.
- ¹⁶M. T. Kibria, A. Ahammed, M. Saad, F. Sony, and S.-U.-I. Hossain, *A Review: Comparative studies on different generation solar cells technology*, tech. rep. ().
- ¹⁷“Progress in Energy Photovoltaic technology and visions for the future”, (2019).
- ¹⁸J. Ramanujam and U. P. Singh, *Copper indium gallium selenide based solar cells - A review*, June 2017.
- ¹⁹V. Bharam, *Advantages and challenges of silicon in the photovoltaic cells*, tech. rep. ().
- ²⁰Top-Alternative-Energy-Sources.com, *Solar Cells - The Three Generations*.
- ²¹S. Facts and Advice, *3 Generations of Solar Cells: Solar Facts and Advice*.
- ²²Q. Chen, N. De Marco, Y. Yang, T. B. Song, C. C. Chen, H. Zhao, Z. Hong, H. Zhou, and Y. Yang, *Under the spotlight: The organic-inorganic hybrid halide perovskite for optoelectronic applications*, July 2015.
- ²³H. L. Wells, “Über die Cäsium- und Kalium-Bleihalogenide”, *Zeitschrift für anorganische Chemie* **3**, 195–210 (1893).
- ²⁴C. K. Møller, *A phase transition in caesium plumbochloride [9]*, 1957.
- ²⁵C. K. Møller, “Crystal structure and photoconductivity of caesium plumbohalides”, *Nature* **182**, 1436 (1958).
- ²⁶D. B. Mitzi, S. Wang, C. A. Feild, C. A. Chess, and A. M. Guloy, “Conducting layered organic-inorganic halides containing 110-oriented perovskite sheets”, *Science* **267**, 1473–1476 (1995).
- ²⁷David B. Mitzi, “Synthesis, Structure, and Properties of Organic-Inorganic Perovskites and Related Materials”, in *Progress in inorganic chemistry*, Vol. 48, edited by K. D. Karlin (John Wiley & Sons, Inc., Hoboken, NJ, USA, Jan. 1999), Ch1.
- ²⁸D. B. Mitzi, “Organic-Inorganic Perovskites Containing Trivalent Metal Halide Layers: The Templating Influence of the Organic Cation Layer”, *Inorganic Chemistry* **39**, 6107–6113 (2000).
- ²⁹A. Kojima, K. Teshima, Y. Shirai, and T. Miyasaka, “Organometal Halide Perovskites as Visible-Light Sensitizers for Photovoltaic Cells”, *Journal of the American Chemical Society* **131**, 6050–6051 (2009).
- ³⁰H. S. Kim, C. R. Lee, J. H. Im, K. B. Lee, T. Moehl, A. Marchioro, S. J. Moon, R. Humphry-Baker, J. H. Yum, J. E. Moser, M. Grätzel, and N. G. Park, “Lead iodide perovskite sensitized all-solid-state submicron thin film mesoscopic solar cell with efficiency exceeding 9%”, *Scientific Reports* **2** (2012).
- ³¹I. Chung, B. Lee, J. He, R. P. Chang, and M. G. Kanatzidis, “All-solid-state dye-sensitized solar cells with high efficiency”, *Nature* **485**, 486–489 (2012).
- ³²W. S. Yang, J. H. Noh, N. J. Jeon, Y. C. Kim, S. Ryu, J. Seo, and S. I. Seok, “High-performance photovoltaic perovskite layers fabricated through intramolecular exchange”, *Science* **348**, 1234–1237 (2015).
- ³³S. D. Stranks, G. E. Eperon, G. Grancini, C. Menelaou, M. J. P. Alcocer, T. Leijtens, L. M. Herz, A. Petrozza, and H. J. Snaith, “Electron-hole diffusion lengths exceeding 1 micrometer in an organometal trihalide perovskite absorber”, *Science* **342**, 341–344 (2013).
- ³⁴Q. Jiang, Z. Chu, P. Wang, X. Yang, H. Liu, Y. Wang, Z. Yin, J. Wu, X. Zhang, and J. You, “Planar-Structure Perovskite Solar Cells with Efficiency beyond 21%”, *Advanced Materials* **29** (2017).
- ³⁵O. of Energy Efficiency Renewable Energy, *Perovskite Solar Cells — Department of Energy*.
- ³⁶E. Smecca, Y. Numata, I. Deretzis, G. Pellegrino, S. Boninelli, T. Miyasaka, A. La Magna, and A. Alberti, “Stability of solution-processed MAPbI₃ and FAPbI₃ layers”, *Physical Chemistry Chemical Physics* **18**, 13413–13422 (2016).
- ³⁷G. E. Eperon, G. M. Paternò, R. J. Sutton, A. Zampetti, A. A. Haghighirad, F. Cacialli, and H. J. Snaith, “Inorganic caesium lead iodide perovskite solar cells”, *Journal of Materials Chemistry A* **3**, 19688–19695 (2015).
- ³⁸P. Wang, X. Zhang, Y. Zhou, Q. Jiang, Q. Ye, Z. Chu, X. Li, X. Yang, Z. Yin, and J. You, “Solvent-controlled growth of inorganic perovskite films in dry environment for efficient and stable solar cells”, *Nature Communications* **9** (2018).
- ³⁹H. S. Jung and N.-G. Park, “Perovskite Solar Cells: From Materials to Devices”, *Small* **11**, 10–25 (2015).

- ⁴⁰G. Xing, N. Mathews, S. Sun, S. S. Lim, Y. M. Lam, M. Grazel, S. Mhaisalkar, and T. C. Sum, "Long-range balanced electron-and hole-transport lengths in organic-inorganic CH₃NH₃PbI₃", *Science* **342**, 344–347 (2013).
- ⁴¹Y. Bi, E. M. Hutter, Y. Fang, Q. Dong, J. Huang, and T. J. Savenije, "Charge Carrier Lifetimes Exceeding 15 μ s in Methylammonium Lead Iodide Single Crystals", *The Journal of Physical Chemistry Letters* **7**, 923–928 (2016).
- ⁴²C. Wehrenfennig, G. E. Eperon, M. B. Johnston, H. J. Snaith, L. M. Herz, C. Wehrenfennig, G. E. Eperon, M. B. Johnston, H. J. Snaith, and L. M. Herz, "High Charge Carrier Mobilities and Lifetimes in Organolead Trihalide Perovskites", *Advanced Materials* **26**, 1584–1589 (2014).
- ⁴³M. B. Johnston and L. M. Herz, "Hybrid Perovskites for Photovoltaics: Charge-Carrier Recombination, Diffusion, and Radiative Efficiencies", *Accounts of Chemical Research* **49**, 146–154 (2016).
- ⁴⁴C. S. Ponseca, T. J. Savenije, M. Abdellah, K. Zheng, A. Yartsev, T. Pascher, T. Harlang, P. Chabera, T. Pullerits, A. Stepanov, J.-P. Wolf, and V. Sundström, "Organometal Halide Perovskite Solar Cell Materials Rationalized: Ultrafast Charge Generation, High and Microsecond-Long Balanced Mobilities, and Slow Recombination", *Journal of the American Chemical Society* **136**, 5189–5192 (2014).
- ⁴⁵B. Suarez, V. Gonzalez-Pedro, T. S. Ripolles, R. S. Sanchez, L. Otero, and I. Mora-Sero, "Recombination Study of Combined Halides (Cl, Br, I) Perovskite Solar Cells", *The Journal of Physical Chemistry Letters* **5**, 1628–1635 (2014).
- ⁴⁶G. E. Eperon, S. D. Stranks, C. Menelaou, M. B. Johnston, L. M. Herz, and H. J. Snaith, "Formamidinium lead trihalide: A broadly tunable perovskite for efficient planar heterojunction solar cells", *Energy and Environmental Science* **7**, 982–988 (2014).
- ⁴⁷K. Miyano, N. Tripathi, M. Yanagida, and Y. Shirai, "Lead Halide Perovskite Photovoltaic as a Model p-i-n Diode", *Accounts of Chemical Research* **49**, 303–310 (2016).
- ⁴⁸G. Giorgi, J.-I. Fujisawa, H. Segawa, and K. Yamashita, "Small Photocarrier Effective Masses Featuring Ambipolar Transport in Methylammonium Lead Iodide Perovskite: A Density Functional Analysis", *The Journal of Physical Chemistry Letters* **4**, 4213–4216 (2013).
- ⁴⁹S. D. Stranks and H. J. Snaith, *Metal-halide perovskites for photovoltaic and light-emitting devices*, May 2015.
- ⁵⁰D. W. DeQuilettes, S. M. Vorpahl, S. D. Stranks, H. Nagaoka, G. E. Eperon, M. E. Ziffer, H. J. Snaith, and D. S. Ginger, "Impact of microstructure on local carrier lifetime in perovskite solar cells", *Science* **348**, 683–686 (2015).
- ⁵¹W.-J. Yin, T. Shi, and Y. Yan, "Superior Photovoltaic Properties of Lead Halide Perovskites: Insights from First-Principles Theory", *The Journal of Physical Chemistry C* **119**, 5253–5264 (2015).
- ⁵²Q. Dong, Y. Fang, Y. Shao, P. Mulligan, J. Qiu, L. Cao, and J. Huang, "Electron-hole diffusion lengths above 175 μ m in solution-grown CH₃NH₃PbI₃ single crystals", *Science* **347**, 967–970 (2015).
- ⁵³P. Dowben, D. Shi, V. Adinolfi, R. Comin, M. Yuan, E. Alarousu, D. ; Shi, V. ; Adinolfi, R. ; Comin, M. ; Yuan, E. ; Alarousu, A. ; Buin, Y. ; Chen, S. ; Hoogland, A. ; Rothenberger, K. ; Katsiev, Y. B. ; Losovyj, X. ; Zhang, P. A. ; Dowben, O. F. ; Mohammed, E. H. ; Sargent, and O. M. Bakr, "Low trap-state density and long carrier diffusion in organolead trihalide perovskite single crystals", *Research Papers in Physics and Astronomy* (2015).
- ⁵⁴S. D. Stranks, V. M. Burlakov, T. Leijtens, J. M. Ball, A. Goriely, and H. J. Snaith, "Recombination Kinetics in Organic-Inorganic Perovskites: Excitons, Free Charge, and Subgap States", *Physical Review Applied* **2** (2014).
- ⁵⁵B. Guzelturk, R. A. Belisle, M. D. Smith, K. Bruening, R. Prasanna, Y. Yuan, V. Gopalan, C. J. Tassone, H. I. Karunadasa, M. D. McGehee, A. M. Lindenberg, B. Guzelturk, A. M. Lindenberg, R. A. Belisle, R. Prasanna, M. D. McGehee, M. D. Smith, H. I. Karunadasa, K. Bruening, C. J. Tassone, Y. Yuan, and V. Gopalan, "Terahertz Emission from Hybrid Perovskites Driven by Ultrafast Charge Separation and Strong Electron-Phonon Coupling", *Advanced Materials* **30**, 1704737 (2018).
- ⁵⁶J. M. Frost, K. T. Butler, F. Brivio, C. H. Hendon, M. Van Schilfgaarde, and A. Walsh, "Atomistic origins of high-performance in hybrid halide perovskite solar cells", *Nano Letters* **14**, 2584–2590 (2014).
- ⁵⁷L. Z. Tan, F. Zheng, S. M. Young, F. Wang, S. Liu, and A. M. Rappe, *Shift current bulk photovoltaic effect in polar materials-hybrid and oxide perovskites and beyond*, Aug. 2016.
- ⁵⁸C. S. Jiang, M. Yang, Y. Zhou, B. To, S. U. Nanayakkara, J. M. Luther, W. Zhou, J. J. Berry, J. Van De Lagemaat, N. P. Padture, K. Zhu, and M. M. Al-Jassim, "Carrier separation and transport in perovskite solar cells studied by nanometre-scale profiling of electrical potential", *Nature Communications* **6** (2015).
- ⁵⁹X. Wu, L. Z. Tan, X. Shen, T. Hu, K. Miyata, M. Tuan Trinh, R. Li, R. Coffee, S. Liu, D. A. Egger, I. Makasyuk, Q. Zheng, A. Fry, J. S. Robinson, M. D. Smith, B. Guzelturk, H. I. Karunadasa, X. Wang, X. Zhu, L. Kronik, A. M. Rappe, and A. M. Lindenberg, "Light-induced picosecond rotational disordering of the inorganic sublattice in hybrid perovskites", *Science Advances* **3** (2017).
- ⁶⁰C. G. Bischak, C. L. Hetherington, H. Wu, S. Aloni, D. F. Ogletree, D. T. Limmer, and N. S. Ginsberg, "Origin of Reversible Photoinduced Phase Separation in Hybrid Perovskites", *Nano Letters* **17**, 1028–1033 (2017).
- ⁶¹A. J. Neukirch, W. Nie, J.-C. Blancon, K. Appavoo, H. Tsai, M. Y. Sfeir, C. Katan, L. Pedesseau, J. Even, J. J. Crochet, G. Gupta, A. D. Mohite, and S. Tretiak, "Polaron Stabilization by Cooperative Lattice Distortion and Cation Rotations in Hybrid Perovskite Materials", *Nano Letters* **16**, 3809–3816 (2016).
- ⁶²K. Miyata, D. Meggiolaro, M. Tuan Trinh, P. P. Joshi, E. Mosconi, S. C. Jones, F. De Angelis, and X. Y. Zhu, "Large polarons in lead halide perovskites", *Science Advances* **3** (2017).
- ⁶³H. Zhu, K. Miyata, Y. Fu, J. Wang, P. P. Joshi, D. Niesner, K. W. Williams, S. Jin, and X. Y. Zhu, "Screening in crystalline liquids protects energetic carriers in hybrid perovskites", *Science* **353**, 1409–1413 (2016).
- ⁶⁴C. C. Stoumpos, C. D. Malliakas, and M. G. Kanatzidis, "Semiconducting tin and lead iodide perovskites with organic cations: Phase transitions, high mobilities, and near-infrared photoluminescent properties", *Inorganic Chemistry* **52**, 9019–9038 (2013).
- ⁶⁵T. Umebayashi, K. Asai, T. Umebayashi, K. Asai, T. Kondo, T. Kondo, and A. Nakao, "Electronic structures of lead iodide based low-dimensional crystals", *Physical Review B - Condensed Matter and Materials Physics* **67** (2003).
- ⁶⁶B.-E. Cohen, M. Wierzbowska, L. Etgar, B.-E. Cohen, L. Etgar, and M. Wierzbowska, "High Efficiency and High Open Circuit Voltage in Quasi 2D Perovskite Based Solar Cells", *Advanced Functional Materials* (2017).

- ⁶⁷M. T. Weller, O. J. Weber, J. M. Frost, and A. Walsh, “Cubic Perovskite Structure of Black Formamidinium Lead Iodide, α -[HC(NH₂)₂]⁺PbI₃⁻, at 298 K”, *The Journal of Physical Chemistry Letters* **6** (2015).
- ⁶⁸R. J. Sutton, M. R. Filip, A. A. Haghighirad, N. Sakai, B. Wenger, F. Giustino, and H. J. Snaith, “Cubic or Orthorhombic? Revealing the Crystal Structure of Metastable Black-Phase CsPbI₃ by Theory and Experiment”, *ACS Energy Letters* **3**, 1787–1794 (2018).
- ⁶⁹Q. Wang, X. Zheng, Y. Deng, J. Zhao, Z. Chen, and J. Huang, “Stabilizing the α -Phase of CsPbI₃ Perovskite by Sulfobetaine Zwitterions in One-Step Spin-Coating Films”, *Joule* **1**, 371–382 (2017).
- ⁷⁰T. Zhang, M. I. Dar, G. Li, F. Xu, N. Guo, M. Grätzel, and Y. Zhao, “Bication lead iodide 2D perovskite component to stabilize inorganic a-CsPbI₃ perovskite phase for high-efficiency solar cells”, *Science Advances* **3** (2017).
- ⁷¹A. Swarnkar, A. R. Marshall, E. M. Sanehira, B. D. Chernomordik, D. T. Moore, J. A. Christians, T. Chakrabarti, and J. M. Luther, “Quantum dot-induced phase stabilization of α -CsPbI₃ perovskite for high-efficiency photovoltaics”, *Science* **354**, 92–95 (2016).
- ⁷²E. M. Sanehira, A. R. Marshall, J. A. Christians, S. P. Harvey, P. N. Ciesielski, L. M. Wheeler, P. Schulz, L. Y. Lin, M. C. Beard, and J. M. Luther, *Enhanced mobility CsPbI₃ quantum dot arrays for record-efficiency, high-voltage photovoltaic cells*, tech. rep. (2017).
- ⁷³A. Hazarika, Q. Zhao, E. A. Gaulding, J. A. Christians, B. Dou, A. R. Marshall, T. Moot, J. J. Berry, J. C. Johnson, and J. M. Luther, “Perovskite Quantum Dot Photovoltaic Materials beyond the Reach of Thin Films: Full-Range Tuning of A-Site Cation Composition”, *ACS Nano* (2018).
- ⁷⁴S. Xiang, W. Li, Y. Wei, J. Liu, H. Liu, L. Zhu, and H. Chen, “The synergistic effect of non-stoichiometry and Sb-doping on air-stable α -CsPbI₃ for efficient carbon-based perovskite solar cells”, *Nanoscale* **10**, 9996–10004 (2018).
- ⁷⁵C. F. J. Lau, X. Deng, J. Zheng, J. Kim, Z. Zhang, M. Zhang, J. Bing, B. Wilkinson, L. Hu, R. Patterson, S. Huang, and A. Ho-Baillie, “Enhanced performance: Via partial lead replacement with calcium for a CsPbI₃ perovskite solar cell exceeding 13% power conversion efficiency”, *Journal of Materials Chemistry A* **6**, 5580–5586 (2018).
- ⁷⁶Y. Hu, F. Bai, X. Liu, Q. Ji, X. Miao, T. Qiu, and S. Zhang, “Bismuth Incorporation Stabilized α -CsPbI₃ for Fully Inorganic Perovskite Solar Cells”, *ACS Energy Letters* **2**, 2219–2227 (2017).
- ⁷⁷A. K. Jena, A. Kulkarni, Y. Sanehira, M. Ikegami, and T. Miyasaka, “Stabilization of α -CsPbI₃ in Ambient Room Temperature Conditions by Incorporating Eu into CsPbI₃”, *Chemistry of Materials* **30**, 6668–6674 (2018).
- ⁷⁸Y. Fan, H. Meng, L. Wang, and S. Pang, “Review of Stability Enhancement for Formamidinium-Based Perovskites”, *Solar RRL* **3**, 1900215 (2019).
- ⁷⁹B. Brunetti, C. Cavallo, A. Ciccioli, G. Gigli, and A. Latini, “On the Thermal and Thermodynamic (In)Stability of Methylammonium Lead Halide Perovskites”, *Nature Scientific Reports* (2016).
- ⁸⁰T. Wu, M. Ahmadi, and B. Hu, “Giant current amplification induced by ion migration in perovskite single crystal photodetectors”, *Journal of Materials Chemistry C* **6**, 8042–8050 (2018).
- ⁸¹Y. Luo, P. Khoram, S. Brittman, Z. Zhu, B. Lai, S. Ping Ong, E. C. Garnett, D. P. Fenning, Y. Luo, Z. Zhu, S. P. Ong, D. P. Fenning, P. Khoram, S. Brittman, E. C. Garnett, and B. Lai, “Direct Observation of Halide Migration and its Effect on the Photoluminescence of Methylammonium Lead Bromide Perovskite Single Crystals”, *Advanced Materials* (2017).
- ⁸²C. Eames, J. M. Frost, P. R. Barnes, B. C. O’Regan, A. Walsh, and M. S. Islam, “Ionic transport in hybrid lead iodide perovskite solar cells”, *Nature Communications* **6** (2015).
- ⁸³J. L. Minns, P. Zajdel, D. Chernyshov, W. Van Beek, and M. A. Green, “Structure and interstitial iodide migration in hybrid perovskite methylammonium lead iodide”, *Nature Communications* **8** (2017).
- ⁸⁴J. Zhao, Y. Deng, H. Wei, X. Zheng, Z. Yu, Y. Shao, J. E. Shield, and J. Huang, “Strained hybrid perovskite thin films and their impact on the intrinsic stability of perovskite solar cells”, *Science Advances* **3** (2017).
- ⁸⁵N. Rolston, K. A. Bush, A. D. Printz, A. Gold-Parker, Y. Ding, M. F. Toney, M. D. McGehee, and R. H. Dauskardt, “Engineering Stress in Perovskite Solar Cells to Improve Stability”, *Advanced Energy Materials* **8**, 1802139 (2018).
- ⁸⁶E. Strelcov, Q. Dong, T. Li, J. Chae, Y. Shao, Y. Deng, A. Gruverman, J. Huang, and A. Centrone, “CH₃NH₃PbI₃ perovskites: Ferroelasticity revealed”, *Science Advances* **3** (2017).
- ⁸⁷Q. Lv, W. He, Z. Lian, J. Ding, Q. Li, and Q. Yan, “Anisotropic moisture erosion of CH₃NH₃PbI₃ single crystals”, *CrystEngComm* **19**, 901–904 (2017).
- ⁸⁸A. M. A. Leguy, Y. Hu, M. Campoy-Quiles, M. I. Alonso, O. J. Weber, P. Azarhoosh, M. van Schilfgaarde, M. T. Weller, T. Bein, J. Nelson, P. Docampo, and P. R. F. Barnes, “Reversible Hydration of CH₃NH₃PbI₃ in Films, Single Crystals, and Solar Cells”, *Chemistry of Materials* **27**, 3397–3407 (2015).
- ⁸⁹S. N. Habisreutinger, T. Leijtens, G. E. Eperon, S. D. Stranks, R. J. Nicholas, and H. J. Snaith, “Carbon nanotube/polymer composites as a highly stable hole collection layer in perovskite solar cells”, *Nano Letters* **14**, 5561–5568 (2014).
- ⁹⁰B. Chaudhary, A. Kulkarni, A. K. Jena, M. Ikegami, Y. Udagawa, H. Kunugita, K. Ema, and T. Miyasaka, “Poly(4-Vinylpyridine)-Based Interfacial Passivation to Enhance Voltage and Moisture Stability of Lead Halide Perovskite Solar Cells”, *ChemSusChem* **10**, 2473–2479 (2017).
- ⁹¹G. Abdelmageed, H. R. Sully, S. Bonabi Naghaddeh, A. El-Hag Ali, S. A. Carter, and J. Z. Zhang, “Improved Stability of Organometal Halide Perovskite Films and Solar Cells toward Humidity via Surface Passivation with Oleic Acid”, *ACS Applied Energy Materials* **1**, 387–392 (2018).
- ⁹²G. Grancini, C. Roldán-Carmona, I. Zimmermann, E. Mosconi, X. Lee, D. Martineau, S. Narbey, F. Oswald, F. De Angelis, M. Graetzel, and M. K. Nazeeruddin, “One-Year stable perovskite solar cells by 2D/3D interface engineering”, *Nature Communications* **8** (2017).
- ⁹³P. Gratia, I. Zimmermann, P. Schouwink, J.-H. Yum, J.-N. Audinot, K. Sivula, T. Wirtz, and M. K. Nazeeruddin, “The Many Faces of Mixed Ion Perovskites: Unraveling and Understanding the Crystallization Process”, *ACS Energy Letters* **2**, 2686–2693 (2017).

- ⁹⁴M. E. Kamminga, G. A. De Wijs, R. W. Havenith, G. R. Blake, and T. T. Palstra, “The Role of Connectivity on Electronic Properties of Lead Iodide Perovskite-Derived Compounds”, *Inorganic Chemistry* **56**, 8408–8414 (2017).
- ⁹⁵L. S. Ramsdell, *Studies on silicon carbide*, tech. rep. (1947).
- ⁹⁶J. J. Cerdà, *Simulation Techniques for Soft Matter Sciences 8: Long range interactions: Direct sum and Ewald summation*, tech. rep. (2007).
- ⁹⁷P. P. Ewald, “Die Berechnung optischer und elektrostatischer Gitterpotentiale”, *Annalen der Physik* **369**, 253–287 (1921).
- ⁹⁸R. J. Tilley, “Defects in Solids”, in *Encyclopedia of inorganic and bioinorganic chemistry* (John Wiley & Sons, Ltd, Chichester, UK, Mar. 2018), pp. 1–23.
- ⁹⁹K. T. Butler, A. Walsh, A. K. Cheetham, and G. Kieslich, *Organised chaos: Entropy in hybrid inorganic-organic systems and other materials*, Sept. 2016.
- ¹⁰⁰C. Caetano, K. T. Butler, and A. Walsh, “Analysis of electrostatic stability and ordering in quaternary perovskite solid solutions”, *Physical Review B* **93**, 144205 (2016).
- ¹⁰¹G. Kieslich, S. Kumagai, K. T. Butler, T. Okamura, C. H. Hendon, S. Sun, M. Yamashita, A. Walsh, and A. K. Cheetham, “Role of entropic effects in controlling the polymorphism in formate ABX₃ metal-organic frameworks”, *Chemical Communications* **51**, 15538–15541 (2015).
- ¹⁰²S. Vela, F. Mota, M. Deumal, R. Suizu, Y. Shuku, A. Mizuno, K. Awaga, M. Shiga, J. J. Novoa, and J. Ribas-Arino, “The key role of vibrational entropy in the phase transitions of dithiazolyl-based bistable magnetic materials”, *Nature Communications* **5**, 1–9 (2014).
- ¹⁰³B. L. Gyorffy, *Coherent-potential approximation for a nonoverlapping-muffin-tin-potential model of random substitutional alloys*, Mar. 1972.
- ¹⁰⁴A. Zunger, S. H. Wei, L. G. Ferreira, and J. E. Bernard, “Special quasirandom structures”, *Physical Review Letters* **65**, 353–356 (1990).
- ¹⁰⁵J. M. Sanchez, F. Ducastelle, and D. Gratias, “Generalized cluster description of multicomponent systems”, *Physica A: Statistical Mechanics and its Applications* **128**, 334–350 (1984).
- ¹⁰⁶F. Brivio, J. M. Frost, J. M. Skelton, A. J. Jackson, O. J. Weber, M. T. Weller, A. R. Goñi, A. M. Leguy, P. R. Barnes, and A. Walsh, “Lattice dynamics and vibrational spectra of the orthorhombic, tetragonal, and cubic phases of methylammonium lead iodide”, *Physical Review B - Condensed Matter and Materials Physics* **92**, 144308 (2015).
- ¹⁰⁷F. Brivio, C. Caetano, and A. Walsh, “Thermodynamic Origin of Photoinstability in the CH₃NH₃Pb(I_{1-x}Br_x)₃ Hybrid Halide Perovskite Alloy”, *Journal of Physical Chemistry Letters* **7**, 1083–1087 (2016).

6 Appendix

6.1 Annotated polytype building code

940 6.1.1 Polytype builder written

Figures 15-21

6.1.2 Polytype builder received from a group member.

Figure 22

6.1.3 POSCAR files generated using the code in Fig 22.

945 Figures 23-25

6.2 Ewald summation method used to calculate electrostatic energy.

Figure 26

6.3 Boltzmann Population Distribution Calculations.

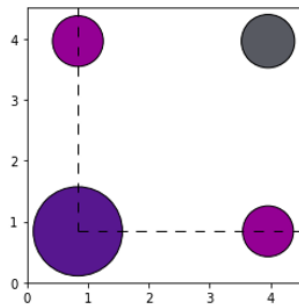
Figure 27

```
In [1]: from ase import Atoms, atoms, Atom
from ase.io import read, write
import ase.visualize
from ase.visualize import ngl
from ase.spacegroup import crystal
from ase.utils import basestring
from ase.build import cut
from ase.build import make_supercell
from ase.visualize.plot import plot_atoms
from ase import geometry
import ase.io.vasp
import numpy as np

import matplotlib.pyplot as plt
import nglview
```

```
In [2]: # Read in and plot the primitive POSCAR cell
CsPbI3 = read('primitive_POSCAR.vasp', format='vasp')
plot_atoms(CsPbI3, radii=0.3, show_unit_cell=1)
```

Out[2]: <matplotlib.axes._subplots.AxesSubplot at 0x274ab92dcf8>



```
In [3]: # check coordinates of atoms
CsPbI3.get_positions()
```

```
Out[3]: array([[0.         , 0.         , 0.         ],
 [3.12172517, 3.12172517, 3.12172517],
 [3.12172517, 3.12172517, 0.         ],
 [0.         , 3.12172517, 3.12172517],
 [3.12172517, 0.         , 3.12172517]])
```

```
In [4]: # check coordinates of cell
CsPbI3.get_cell()
```

```
Out[4]: Cell([6.243450339272835, 6.243450339272835, 6.243450339272835])
```

```
In [5]: from IPython.display import Image
Image(filename='perovskite_polytypes.png', width=400)
```

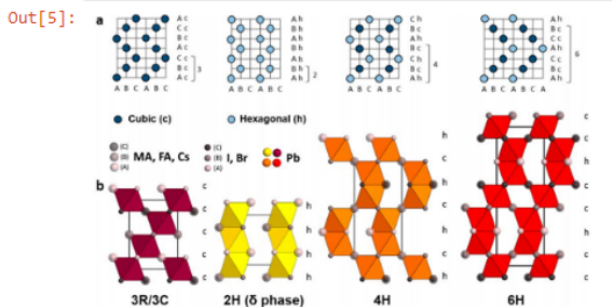


Figure 1. (a) Comparison of the AX₃ stacking sequence between different lead halide perovskite polytypes, and (b) the representation of their refined single-crystal structure showing the different possible arrangements and the connectivity of the octahedra (reprinted from [1]).

```
In [6]: #add I and Cs atoms
l=CsPbI3.cell[(0,0)]
extra_Cs=Atoms('Cs7',[(0,1,0),(0,1,1),(1,1,1),(1,0,1),(1,0,0),(1,1,0),(0,0,1)])
extra_Cs.get_positions()
extra_Cs.get_atomic_numbers()
extra_Cs.get_chemical_symbols()

extra_I=Atoms('I3',[(1/2,1,1/2),(1,1/2,1/2),(1/2,1/2,1)])
extra_I.get_positions()
extra_I.get_atomic_numbers()
extra_I.get_chemical_symbols()
```

Figure 15: Polytype builder realised during this project. Part 1.

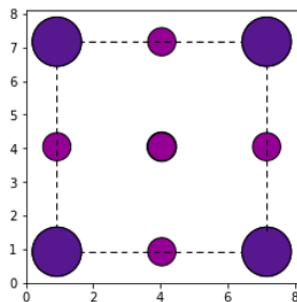
```
Out[6]: array([53, 53, 53])
```

```
In [7]: #combine structures
full_octahedra=CspBI3.copy()
full_octahedra.extend(extra-Cs)
full_octahedra.extend(extra-I)
full_octahedra.get_positions()
```

```
Out[7]: array([[0.         , 0.         , 0.         ],
 [3.12172517, 3.12172517, 3.12172517],
 [3.12172517, 3.12172517, 0.         ],
 [0.         , 3.12172517, 3.12172517],
 [3.12172517, 0.         , 3.12172517],
 [0.         , 6.24345034, 0.         ],
 [0.         , 6.24345034, 6.24345034],
 [6.24345034, 6.24345034, 6.24345034],
 [6.24345034, 0.         , 6.24345034],
 [6.24345034, 0.         , 0.         ],
 [6.24345034, 6.24345034, 0.         ],
 [0.         , 0.         , 6.24345034],
 [3.12172517, 6.24345034, 3.12172517],
 [6.24345034, 3.12172517, 3.12172517],
 [3.12172517, 3.12172517, 6.24345034]])
```

```
In [8]: plot_atoms(full_octahedra,radii=0.3, show_unit_cell=2,rotation=('0x,0y,0z'))
```

```
Out[8]: <matplotlib.axes._subplots.AxesSubplot at 0x274ac243048>
```



```
In [9]: full_octahedra.get_positions()
```

```
Out[9]: array([[0.         , 0.         , 0.         ],
 [3.12172517, 3.12172517, 3.12172517],
 [3.12172517, 3.12172517, 0.         ],
 [0.         , 3.12172517, 3.12172517],
 [3.12172517, 0.         , 3.12172517],
 [0.         , 6.24345034, 0.         ],
 [0.         , 6.24345034, 6.24345034],
 [6.24345034, 6.24345034, 6.24345034],
 [6.24345034, 0.         , 6.24345034],
 [6.24345034, 0.         , 0.         ],
 [6.24345034, 6.24345034, 0.         ],
 [0.         , 0.         , 6.24345034],
 [3.12172517, 6.24345034, 3.12172517],
 [6.24345034, 3.12172517, 3.12172517],
 [3.12172517, 3.12172517, 6.24345034]])
```

```
In [10]: A_octahedra=full_octahedra.copy()
B_octahedra=full_octahedra.copy()
```

```
In [11]: # rotate the unit cell to be along 111
# (I've used theta_2 = 90 - arctan(sqrt(2)) since this will make the iodine atoms lie horizontally)
theta_1 = 45
theta_2 = 90 - np.degrees(np.arctan(np.sqrt(2)))
A_octahedra.rotate(theta_1, 'x', center='COU', rotate_cell=False)
A_octahedra.rotate(theta_2, 'z', center='COU', rotate_cell=False)
```

```
In [12]: # plot to check building block A
plot_atoms(A_octahedra,radii=0.3, show_unit_cell=2,rotation=('0x,0y,0z'))
```

```
Out[12]: <matplotlib.axes._subplots.AxesSubplot at 0x274ac8c2160>
```

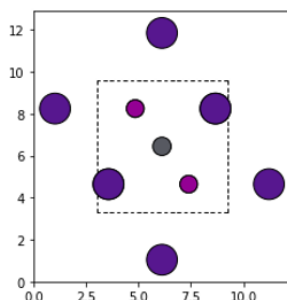
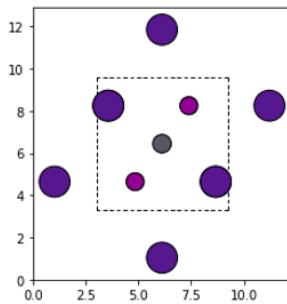


Figure 16: Polytype builder realised during this project. Part 2.

```
In [13]: B_octahedra.rotate(-theta_1, 'x', center='COU', rotate_cell=False)
B_octahedra.rotate(-theta_2, 'z', center='COU', rotate_cell=False)
```

```
In [14]: # plot to check building block B
plot_atoms(B_octahedra,radii=0.3, show_unit_cell=2,rotation=('0x,0y,0z'))
```

```
Out[14]: <matplotlib.axes._subplots.AxesSubplot at 0x274acaf20b8>
```



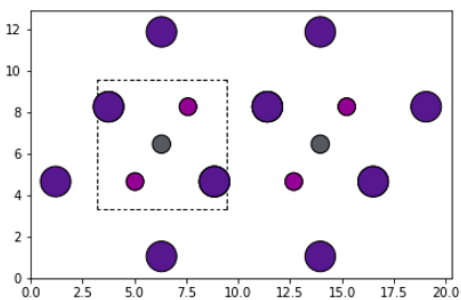
```
In [15]: # building the corner sharing structure 3C
B1_octahedra=B_octahedra.copy() #to copy the structure and B_octahedra and save it under B1
```

```
In [16]: #to translate B1 horizontally
B1_octahedra.translate([np.sqrt(3)*l/(np.sqrt(2)), 0, l/(np.sqrt(2))])
#B1_octahedra.translate([np.sqrt(3)*L/(np.sqrt(2)), 0, 0])
B1_octahedra.get_positions()
```

```
Out[16]: array([[ 5.6706031 ,  1.3193963 ,  7.53651124],
 [10.76835895,  3.12172517,  7.53651124],
 [ 9.49391999,  1.3193963 ,  5.32911821],
 [ 8.21948102,  4.92405404,  7.53651124],
 [ 9.49391999,  1.3193963 ,  9.74390428],
 [ 8.21948102,  4.92405404,  3.12172517],
 [10.76835895,  8.52871177,  7.53651124],
 [15.86611481,  4.92405404,  7.53651124],
 [13.31723688,  1.3193963 , 11.95129732],
 [10.76835895, -2.28526143,  7.53651124],
 [13.31723688,  1.3193963 ,  3.12172517],
 [ 8.21948102,  4.92405404, 11.95129732],
 [12.04279792,  4.92405404,  5.32911821],
 [13.31723688,  1.3193963 ,  7.53651124],
 [12.04279792,  4.92405404,  9.74390428]])
```

```
In [17]: #add block B to the translated B1 block
B1_octahedra.extend(B_octahedra)
plot_atoms(B1_octahedra,radii=0.3, show_unit_cell=2, rotation=('0x,0y,0z'))
```

```
Out[17]: <matplotlib.axes._subplots.AxesSubplot at 0x274acd2d550>
```



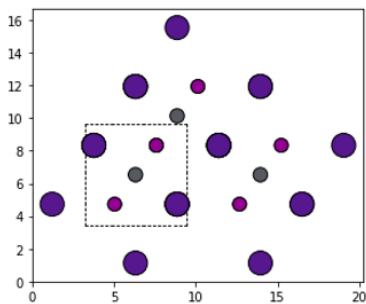
```
In [18]: B1_octahedra.get_positions()
```

Figure 17: Polytype builder realised during this project. Part 3.

```
Out[18]: array([[ 5.6706031 ,  1.3193963 ,  7.53651124],
 [10.76835895,  3.12172517,  7.53651124],
 [ 9.49391999,  1.3193963 ,  5.32911821],
 [ 8.21948102,  4.92405404,  7.53651124],
 [ 9.49391999,  1.3193963 ,  9.74390428],
 [ 8.21948102,  4.92405404,  3.12172517],
 [10.76835895,  8.52871177,  7.53651124],
 [15.86611481,  4.92405404,  7.53651124],
 [13.31723688,  1.3193963 , 11.95129732],
 [10.76835895, -2.28526143,  7.53651124],
 [13.31723688,  1.3193963 ,  3.12172517],
 [ 8.21948102,  4.92405404, 11.95129732],
 [12.04279792,  4.92405404,  5.32911821],
 [13.31723688,  1.3193963 ,  7.53651124],
 [12.04279792,  4.92405404,  9.74390428],
 [-1.97603069,  1.3193963 ,  3.12172517],
 [ 3.12172517,  3.12172517,  3.12172517],
 [ 1.84728621,  1.3193963 ,  0.91433213],
 [ 0.57284724,  4.92405404,  3.12172517],
 [ 1.84728621,  1.3193963 ,  5.32911821],
 [ 0.57284724,  4.92405404, -1.2930609 ],
 [ 3.12172517,  8.52871177,  3.12172517],
 [ 8.21948102,  4.92405404,  3.12172517],
 [ 5.6706031 ,  1.3193963 ,  7.53651124],
 [ 3.12172517, -2.28526143,  3.12172517],
 [ 5.6706031 ,  1.3193963 , -1.2930609 ],
 [ 0.57284724,  4.92405404,  7.53651124],
 [ 4.39616413,  4.92405404,  0.91433213],
 [ 5.6706031 ,  1.3193963 ,  3.12172517],
 [ 4.39616413,  4.92405404,  5.32911821]])
```

```
In [19]: #adding a 3rd block. First B renamed B2 again, then translated across and added to B1, composed of two blocks with one of them
#translated
B2_octahedra=B_octahedra.copy()
B2_octahedra.translate([np.sqrt(3)*1/(3*np.sqrt(2)), 1/(np.sqrt(3)), 1/((np.sqrt(2)))]])
B2_octahedra.extend(B1_octahedra)
plot_atoms(B2_octahedra,radii=0.3, show_unit_cell=2, rotation=('0x,0y,0z'))
```

```
Out[19]: <matplotlib.axes._subplots.AxesSubplot at 0x274acfaa940>
```



```
In [20]: #adding 4th block
B3_octahedra=B_octahedra.copy()
B3_octahedra.translate([2*np.sqrt(3)*1/(3*np.sqrt(2)), 2*1/(np.sqrt(3)), 0])
B3_octahedra.extend(B2_octahedra)
plot_atoms(B3_octahedra,radii=0.3, show_unit_cell=2, rotation=('0x,0y,0z'))
```

```
Out[20]: <matplotlib.axes._subplots.AxesSubplot at 0x274ad24db38>
```

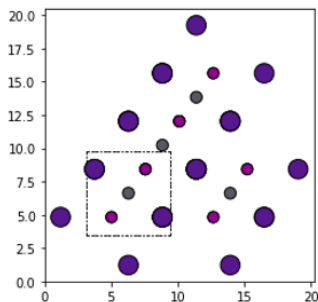


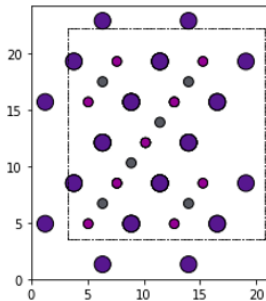
Figure 18: Polytype builder realised during this project. Part 4.

```
In [21]: #adding 5th block, the same as on the base composed of two blocks, it's called B1
B4_octahedra=B1_octahedra.copy()
B4_octahedra.translate([0, 3*1/(np.sqrt(3)), 1/((np.sqrt(2)))]])
B4_octahedra.extend(B3_octahedra)

#change the unit cell borders
B4_octahedra.set_cell([2.8*1, 3*1, 2.8*1])

#delete duplicate atoms, we need to choose to delete the Cs and not the I which is naturally removed
ase.geometry.get_duplicate_atoms(B4_octahedra, cutoff=0.5, delete=False)
plot_atoms(B4_octahedra, radii=0.3, show_unit_cell=2, rotation=('0x,0y,0z'))
```

Out[21]: <matplotlib.axes._subplots.AxesSubplot at 0x274ae4a27f0>



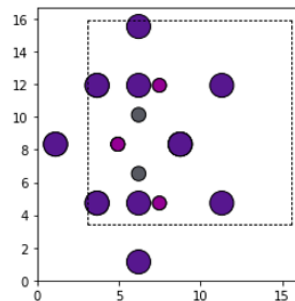
```
In [22]: #download the structure to check it in VESTA
ase.io.vasp.write_vasp('3C_structure.vasp', B4_octahedra, direct=False, sort=True, long_format=True, vasp5=True)
```

```
In [23]: # building the face sharing structure 2H
B3_octahedra=B_octahedra.copy() #to copy the structure and B_octahedra and save it under B1
```

```
In [24]: #to translate B3 vertically
B3_octahedra.translate([0, 1/(np.sqrt(3)), 1/((np.sqrt(2)))]])
#add block A to the translated B3 block
B3_octahedra.extend(A_octahedra)

B3_octahedra.set_cell([2*1, 2*1, 2*1])
ase.io.vasp.write_vasp('2H1_structure.vasp', B3_octahedra, direct=False, sort=True, long_format=True, vasp5=True)
plot_atoms(B3_octahedra, radii=0.3, show_unit_cell=2, rotation=('0x,0y,0z'))
```

Out[24]: <matplotlib.axes._subplots.AxesSubplot at 0x274ae537908>



```
In [25]: # building the face sharing structure 2H
A4_octahedra=A_octahedra.copy() #to copy the structure and B_octahedra and save it under B1
#to translate B3 vertically again
A4_octahedra.translate([0, 2*1/(np.sqrt(3)), 1/((np.sqrt(2)))]])
#add block B3 to the translated B3 block
A4_octahedra.extend(B3_octahedra)
plot_atoms(A4_octahedra, radii=0.3, show_unit_cell=2, rotation=('0x,0y,0z'))
```

Out[25]: <matplotlib.axes._subplots.AxesSubplot at 0x274aef2c780>

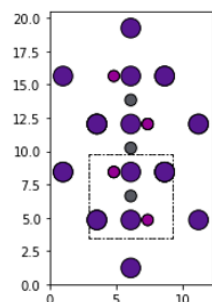
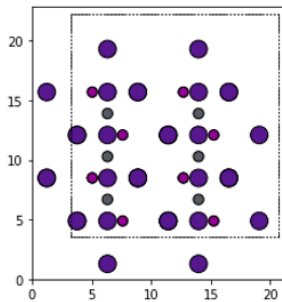


Figure 19: Polytype builder realised during this project. Part 5.

```
In [26]: #adding the next column
A5_octahedra=A4_octahedra.copy()
A5_octahedra.translate([np.sqrt(3)*1/(np.sqrt(2)), 0, 0])
A5_octahedra.extend(A4_octahedra)
#delete duplicate atoms
ase.geometry.get_duplicate_atoms(A5_octahedra, cutoff=0.5, delete=True)
#change the unit cell borders
A5_octahedra.set_cell([2.8*1, 3*1, 2.8*1])
plot_atoms(A5_octahedra,radii=0.3, show_unit_cell=2, rotation=('0x,0y,0z'))
```

Out[26]: <matplotlib.axes._subplots.AxesSubplot at 0x274aeae38d0>



```
In [27]: # build the 4H structure
B5_octahedra=B1_octahedra.copy() #bottom 2 blocks
B6_octahedra=B_octahedra.copy()
B6_octahedra.translate([-2*np.sqrt(3)*1/(3*np.sqrt(2)), 1/(np.sqrt(3)), 0]) #2nd row Left
B5_octahedra.extend(B6_octahedra)
B7_octahedra=B_octahedra.copy() #2nd row right
B7_octahedra.translate([np.sqrt(3)*1/(3*np.sqrt(2)), 1/(np.sqrt(3)), 0])
B5_octahedra.extend(B7_octahedra)
A6_octahedra=A_octahedra.copy() #3rd row Left
A6_octahedra.translate([-2*np.sqrt(3)*1/(3*np.sqrt(2)), 2*1/(np.sqrt(3)), 0])
B5_octahedra.extend(A6_octahedra)
A7_octahedra=A_octahedra.copy() #3rd row right
A7_octahedra.translate([np.sqrt(3)*1/(3*np.sqrt(2)), 2*1/(np.sqrt(3)), 0])
B5_octahedra.extend(A7_octahedra)
A8_octahedra=A_octahedra.copy() #4th row Left
A8_octahedra.translate([0, 3*1/(np.sqrt(3)), 0])
B5_octahedra.extend(A8_octahedra)
A9_octahedra=A_octahedra.copy() #4th row right
A9_octahedra.translate([3*np.sqrt(3)*1/(3*np.sqrt(2)), 3*1/(np.sqrt(3)), 0])
B5_octahedra.extend(A9_octahedra)
B8_octahedra=B1_octahedra.copy() #row 5 both octahedra
B8_octahedra.translate([0, 4*1/(np.sqrt(3)), 0])
B5_octahedra.extend(B8_octahedra)
B9_octahedra=B1_octahedra.copy()
B9_octahedra.translate([-2*np.sqrt(3)*1/(3*np.sqrt(2)), 5*1/(np.sqrt(3)), 0]) #6th row both
B5_octahedra.extend(B9_octahedra)
#delete duplicate atoms
ase.geometry.get_duplicate_atoms(B5_octahedra, cutoff=0.5, delete=True)
plot_atoms(B5_octahedra,radii=0.3, show_unit_cell=2, rotation=('0x,0y,0z'))
```

Out[27]: <matplotlib.axes._subplots.AxesSubplot at 0x274af840128>

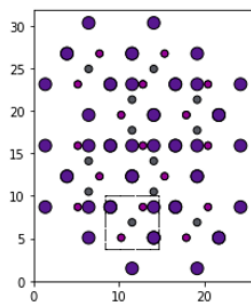
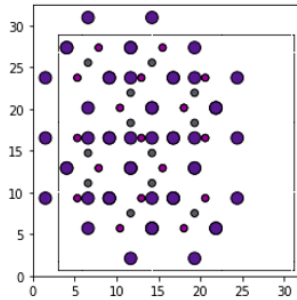


Figure 20: Polytype builder realised during this project. Part 6.

```
In [28]: #change the unit cell borders
B5_octahedra.set_cell([4.5*1, 4.5*1, 5*1])
B5_octahedra.translate([np.sqrt(3)*1/(3*np.sqrt(2))+3, 1/(np.sqrt(3)), 1/(np.sqrt(3))])
plot_atoms(B5_octahedra,radii=0.3, show_unit_cell=2, rotation=('0x,0y,0z'))
ase.io.vasp.write_vasp('4H_structure.vasp', B5_octahedra, direct=False, sort=True, long_format=True, vasp5=True)
```



```
In [29]: #Last one 6H
A10_octahedra=A_octahedra.copy()
A11_octahedra=A_octahedra.copy()
A11_octahedra.translate([-np.sqrt(3)*1/(3*np.sqrt(2)), 1/(np.sqrt(3)), 0])
A10_octahedra.extend(A11_octahedra)
B10_octahedra=B_octahedra.copy()
B10_octahedra.translate([-np.sqrt(3)*1/(3*np.sqrt(2)), 2*1/(np.sqrt(3)), 0]) #2nd row Left
A10_octahedra.extend(B10_octahedra)
B11_octahedra=B_octahedra.copy()
B11_octahedra.translate([0, 3*1/(np.sqrt(3)), 0])
A10_octahedra.extend(B11_octahedra)
B12_octahedra=B_octahedra.copy()
B12_octahedra.translate([np.sqrt(3)*1/(3*np.sqrt(2)), 4*1/(np.sqrt(3)), 0])
A10_octahedra.extend(B12_octahedra)
A12_octahedra=A_octahedra.copy()
A12_octahedra.translate([np.sqrt(3)*1/(3*np.sqrt(2)), 5*1/(np.sqrt(3)), 0])
A10_octahedra.extend(A12_octahedra)
A13_octahedra=A_octahedra.copy()
A13_octahedra.translate([0, 6*1/(np.sqrt(3)), 0])
A10_octahedra.extend(A13_octahedra)
A14_octahedra=A10_octahedra.copy()
A14_octahedra.translate([np.sqrt(3)*1/(np.sqrt(2)), 0, 0])
A14_octahedra.extend(A10_octahedra)

#delete duplicate atoms
ase.geometry.get_duplicate_atoms(A14_octahedra, cutoff=0.5, delete=True)

#change the unit cell borders
A14_octahedra.set_cell([3.2*1, 6*1, 3.2*1])
A14_octahedra.translate([2, 0, 0])

plot_atoms(A14_octahedra,radii=0.3, show_unit_cell=2, rotation=('0x,0y,0z'))
```

Out[29]: <matplotlib.axes._subplots.AxesSubplot at 0x274b04cbe10>

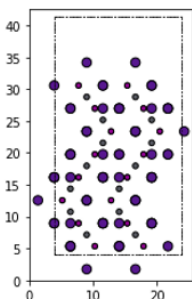


Figure 21: Polytype builder realised during this project. Part 7.

```

#####
LC = 6.2904720703589856 #Lattice constant (cubic)
savefilename = 'POSCAR_TEST'
#####

#####
import numpy as np

def list2str(inputList):
    return str("%.15f" % inputList[0]) + ' ' + str("%.15f" % inputList[1]) + ' ' + str("%.15f" % inputList[2]) + '\n'

def generateAtoms(atom, vector, sAtom):
    tempStr = ''
    for i in range(NoLayer):
        temp = list2str(atom + vector * i + shift * sAtom[i] )
        tempStr += temp
    return(tempStr)

def readPOS():
    a = open('POS')
    b = a.readlines()
    data = []
    for i in range(len(b)):
        if '#' in b[i]:
            pass
        elif len(b[i].split()) == 0:
            pass
        else:
            #print(b[i].split()[:-1])
            temp = list(map(int,b[i].split()[:-1]))
            data.append(temp)
    Cs = data[0]
    Sn = data[1]
    I1 = data[2]
    I2 = data[3]
    I3 = data[4]
    NoLayer = len(Cs)
    #print(NoLayer)
    return(NoLayer,Cs,Sn,I1,I2,I3)

#####
NoLayer, sCs, sSn, sI1, sI2, sI3 = readPOS()
noAtom = np.asarray([1,1,3]) * NoLayer

shift = np.asarray([1.0/3,1.0/3,0.0])
lat1 = LC * np.asarray([np.sqrt(2) , 0, 0])
lat2 = LC * np.asarray([np.sqrt(2)/2, np.sqrt(6)/2, 0])
lat3 = LC * np.asarray([ 0, 0, np.sqrt(3)/3 * NoLayer])

b = 'Perovskite Stacking Fault\n'
b += '1.0000000000000000\n'
b += ' ' + list2str(lat1)
b += ' ' + list2str(lat2)
b += ' ' + list2str(lat3)
b += ' Cs Sn I\n' #You may change this line
b += ' ' + ' '.join(list(map(str,noAtom))) + '\n'
b += 'direct\n'

Cs = np.asarray([0,0,0])
Sn = np.asarray([2.0/3,2.0/3,1.0/NoLayer/2])
I1 = np.asarray([0.5,0.0,0.0])
I2 = np.asarray([0.0,0.5,0.0])
I3 = np.asarray([0.5,0.5,0.0])
vector = np.asarray([1.0/3,1.0/3,1.0/NoLayer])

b += generateAtoms(Cs,vector,sCs)
b += generateAtoms(Sn,vector,sSn)
b += generateAtoms(I1,vector,sI1)
b += generateAtoms(I2,vector,sI2)
b += generateAtoms(I3,vector,sI3)

a = open(savefilename,'w')
a.write(b)
a.close()
#####

```

Figure 22: Code written by a group member.


```

*POSCAR_12 - Notepad
File Edit Format View Help
Perovskite Stacking Fault
1.0000000000000000
  8.896070915630840    0.000000000000000    0.000000000000000
  4.448035457815420    7.704223406804198    0.000000000000000
  0.000000000000000    0.000000000000000    43.581668917818995
  Cs Sn I
  12 12 36
direct
0.000000000000000    0.000000000000000    0.000000000000000
0.333333333333333    0.333333333333333    0.083333333333333
1.000000000000000    1.000000000000000    0.166666666666667
1.666666666666667    1.666666666666667    0.250000000000000
1.333333333333333    1.333333333333333    0.333333333333333
2.000000000000000    2.000000000000000    0.416666666666667
1.666666666666667    1.666666666666667    0.500000000000000
2.333333333333333    2.333333333333333    0.583333333333333
2.666666666666667    2.666666666666667    0.666666666666667
3.000000000000000    3.000000000000000    0.750000000000000
3.333333333333333    3.333333333333333    0.833333333333333
3.666666666666667    3.666666666666667    0.916666666666667
0.666666666666667    0.666666666666667    0.041666666666667
0.666666666666667    0.666666666666667    0.125000000000000
1.333333333333333    1.333333333333333    0.208333333333333
2.000000000000000    2.000000000000000    0.291666666666667
2.666666666666667    2.666666666666667    0.375000000000000
2.333333333333333    2.333333333333333    0.458333333333333
2.000000000000000    2.000000000000000    0.541666666666667
3.000000000000000    3.000000000000000    0.625000000000000
3.333333333333333    3.333333333333333    0.708333333333333
3.666666666666667    3.666666666666667    0.791666666666667
4.000000000000000    4.000000000000000    0.875000000000000
4.333333333333333    4.333333333333333    0.958333333333333
0.500000000000000    0.000000000000000    0.000000000000000
0.833333333333333    0.333333333333333    0.083333333333333
1.500000000000000    1.000000000000000    0.166666666666667
2.166666666666667    1.666666666666667    0.250000000000000
1.833333333333333    1.333333333333333    0.333333333333333
2.500000000000000    2.000000000000000    0.416666666666667
2.166666666666667    1.666666666666667    0.500000000000000
2.833333333333333    2.333333333333333    0.583333333333333
3.166666666666667    2.666666666666667    0.666666666666667
3.500000000000000    3.000000000000000    0.750000000000000
3.833333333333333    3.333333333333333    0.833333333333333
4.166666666666667    3.666666666666667    0.916666666666667
0.000000000000000    0.500000000000000    0.000000000000000
0.333333333333333    0.833333333333333    0.083333333333333
1.000000000000000    1.500000000000000    0.166666666666667
1.666666666666667    2.166666666666667    0.250000000000000
1.333333333333333    1.833333333333333    0.333333333333333
2.000000000000000    2.500000000000000    0.416666666666667
1.666666666666667    2.166666666666667    0.500000000000000
2.333333333333333    2.833333333333333    0.583333333333333
2.666666666666667    3.166666666666667    0.666666666666667
3.000000000000000    3.500000000000000    0.750000000000000
3.333333333333333    3.833333333333333    0.833333333333333
3.666666666666667    4.166666666666667    0.916666666666667
0.500000000000000    0.500000000000000    0.000000000000000
0.833333333333333    0.833333333333333    0.083333333333333
1.500000000000000    1.500000000000000    0.166666666666667
2.166666666666667    2.166666666666667    0.250000000000000
1.833333333333333    1.833333333333333    0.333333333333333
2.500000000000000    2.500000000000000    0.416666666666667
2.166666666666667    2.166666666666667    0.500000000000000
2.833333333333333    2.833333333333333    0.583333333333333
3.166666666666667    3.166666666666667    0.666666666666667
3.500000000000000    3.500000000000000    0.750000000000000
3.833333333333333    3.833333333333333    0.833333333333333
4.166666666666667    4.166666666666667    0.916666666666667

```

Figure 25: POSCAR file generated using the code in Fig 22 for the 12H structure.

```

In [1]: import pymatgen
import math
import numpy as np
import array as arr
#from pymatgen.io.vasp import Poscar
from pymatgen import Structure
from pymatgen.alchemy.materials import TransformedStructure
#from pymatgen.transformations.standard_transformations import
from pymatgen.analysis.bond_valence import BVAnalyzer
from pymatgen.analysis.ewald import EwaldSummation
bva = BVAnalyzer()
from pymatgen.transformations.standard_transformations import SubstitutionTransformation, RemoveSpeciesTransformation

In [2]: poscar_structure = '''Perovskite Stacking Fault
1.0000000000000000
  8.896070915630840    0.0000000000000000    0.0000000000000000
  4.448035457815420    7.704223406804198    0.0000000000000000
  0.0000000000000000    0.0000000000000000    7.263611486303165
Cs  Pb  I
 2   2   6
direct
0.0000000000000000    0.0000000000000000    0.0000000000000000
0.3333333333333333    0.3333333333333333    0.5000000000000000
0.6666666666666667    0.6666666666666667    0.2500000000000000
0.6666666666666667    0.6666666666666667    0.7500000000000000
0.5000000000000000    0.0000000000000000    0.0000000000000000
0.8333333333333333    0.3333333333333333    0.5000000000000000
0.0000000000000000    0.5000000000000000    0.0000000000000000
0.3333333333333333    0.8333333333333333    0.5000000000000000
0.5000000000000000    0.5000000000000000    0.0000000000000000
0.8333333333333333    0.8333333333333333    0.5000000000000000
'''

In [3]: trans = []
structure = Structure.from_str(poscar_structure, fmt='POSCAR')
structure.add_oxidation_state_by_guess()

In [4]: esum = EwaldSummation(structure)

In [5]: #The resulting total electrostatic energy before dividing by the number of (ABX3) units in the unit cell so that the numbers
# can be compared.
print(esum.total_energy)

-52.564239883545284

```

Figure 26: Ewald summation method used to calculate the electrostatic energy of different polytypes. In this example, the electrostatic energy of the 2H polytype of CsPbI₃ is calculated.

```
In [1]: import pymatgen
import math
import numpy as np
import array as arr
from pymatgen.io.vasp import Poscar
from pymatgen import Structure
from pymatgen.alchemy.materials import TransformedStructure
from pymatgen.transformations.standard_transformations import
from pymatgen.analysis.bond_valence import BVAnalyzer
from pymatgen.analysis.ewald import EwaldSummation
bva = BVAnalyzer()
from pymatgen.transformations.standard_transformations import SubstitutionTransformation, RemoveSpeciesTransformation
```

```
In [2]: #Boltzmann Population Distribution Calculation
kB=8.617333262E-5 # Boltzmann constant in eV K^-1
T=3000 # temperature in K
B=1/(kB*T)

#E gives the relative electrostatic energies of different polytypes at 298K
E0=0 #cubic/3C
E1=0.410277905#2H
E2=0.195070535 #4H
E3=0.129682785 #6H
E4=0.064858376 #12H

Z0=np.exp(-B*E0)
Z1=np.exp(-B*E1)
Z2=np.exp(-B*E2)
Z3=np.exp(-B*E3)
Z4=np.exp(-B*E4)

Z=np.sum(Z0+Z1+Z3+Z4)
```

```
In [3]: # The Boltzmann Population Distribution in the range [0-1]
print((1/Z)* np.exp((-0/(kB*T))))

0.38637104424495383
```

Figure 27: Boltzmann Population Distribution Calculations on Python. In this example, CsPbI₃ Boltzmann Population Distribution is calculated at 3000K.